

Temperature-dependent elastic properties of binary and multicomponent *high-entropy* refractory carbides

D.G. Sangiovanni,^{1*} F. Tasnádi,¹ T. Harrington,² K.S. Vecchio,² I.A. Abrikosov^{1,3}

¹ Theoretical Physics Division, Department of Chemistry, Physics, and Biology (IFM), Linköping University, SE 581 83 Linköping, Sweden

² Department of NanoEngineering, University of California, San Diego, La Jolla, CA 92093, USA

³ Materials Modeling and Development Laboratory, National University of Science and Technology “MISIS”, 119049 Moscow, Russia

Available information concerning the elastic moduli of refractory carbides at temperatures (T) of relevance for practical applications is sparse and/or inconsistent. We carry out *ab initio* molecular dynamics (AIMD) simulations at T = 300, 600, 900, and 1200 K to determine the temperature-dependences of the elastic constants of rocksalt-structure (B1) TiC, ZrC, HfC, VC, and TaC compounds as well as multicomponent *high-entropy* carbides (Ti,Zr,Hf,Ta,W)C and (V,Nb,Ta,Mo,W)C. The second order elastic constants are calculated by least-square fitting of the analytical expressions of stress vs. strain relationships to simulation results obtained from three tensile and three shear deformation modes. Moreover, we employ sound velocity measurements to evaluate the bulk, shear, elastic moduli and Poisson's ratios of single-phase B1 (Ti,Zr,Hf,Ta,W)C and (V,Nb,Ta,Mo,W)C at ambient conditions. Our experimental results are in excellent agreement with the values obtained by AIMD simulations. In comparison with the predictions of previous *ab initio* calculations – where the extrapolation of finite-temperature elastic properties accounted for thermal expansion while neglecting intrinsic vibrational effects – AIMD simulations produce a softening of elastic moduli with T in closer agreement with experiments. Results of our simulations show that TaC is the system which exhibits the highest elastic resistances to both tensile and shear deformation up to 1200 K, and identify the high-entropy (V,Nb,Ta,Mo,W)C system as candidate for applications that require good ductility and toughness at room as well as elevated temperatures.

* Corresponding author: davide.sangiovanni@liu.se

1. Introduction

Elastic moduli and elastic stiffness constants of crystals have primary importance in materials design and materials discovery. For example, the search of novel solid crystal phases with potentially new properties includes verifying the Born von Kármán conditions of elastic stiffness constants for mechanical stability [1]. The temperature variation of the elastic anisotropy has a fundamental impact on the material's microstructure evolution and thus on observed age hardening mechanisms in ceramic coatings [2, 3]. Hardness and toughness of refractory ceramics are discussed in terms of the residual stress in the material, which is evaluated through the knowledge of elastic stiffness constants. Indeed, *ab initio* investigations have shown that the predicted elastic constants may vary up to $\approx 20\%$ depending on deformation path, strain range, and order of the polynomial used to fit energy vs. strain curves [4]. In regard to the identification of materials with superior mechanical or structural performance, the observed trends in hardness [5, 6], strength [7, 8], toughness [9-11] and ductility [7, 8, 12, 13] are often correlated to trends in *elastic* constants of the materials.

The elastic constants of solid crystal phases can be efficiently screened by high-throughput *ab initio* calculations at 0 kelvin [14]. In contrast, realistic modeling and evaluation of mechanical properties as hardness and toughness, which would require simulation boxes with volumes of the order $\approx 10^3\text{--}10^5\text{ nm}^3$ [15], is currently unfeasible for first-principles methods. For this reason, *ab initio* calculated polycrystalline elastic moduli, such as shear modulus and Poisson ratio, are widely employed to design empirical indicators of hardness and toughness of compounds and alloys [9, 16-20] which, combined with the progress in machine-learning approaches [20-22], can lead to an increasingly more rapid identification of solids with enhanced mechanical performance.

In the case of refractory carbide, nitride, and boride ceramics, properties as hardness and toughness are of paramount importance, especially for high-temperature applications. Despite this, the elastic constants of these refractory ceramics have been primarily evaluated at 0 K. *Ab initio* estimations of elastic constants at finite temperatures are often done using static calculations at cell volumes determined in the quasiharmonic approximation for the thermal expansion (see, e.g., [23-

27]). However, explicit inclusion of lattice vibrations in theoretical modeling is shown to result in significant differences in second-order elastic moduli and a change of elastic anisotropy of materials at moderate or high temperatures [28, 29]. *Ab initio* molecular dynamics (AIMD) simulations, which inherently reproduce anharmonic vibrational effects, provide more reliable predictions of elastic constants at elevated temperature [29-31].

Recently, we have reported on an *ab initio* molecular dynamics (AIMD) approach for computing stress/strain curves of single-crystal B1 ceramics subject to tensile and shear deformation at any temperature of interest [32-34]. The simulations employ deformations well beyond the elastic limit conventionally used to calculate the elastic constants [28-31], and allow evaluating mechanical properties including, e.g., ideal strengths, moduli of resilience, toughness, and elongation at fracture. The method detailed in Refs. [32-34] has been used to produce the full stress/strain curves in rocksalt-structure (B1) transition-metal carbides (TMC) at temperatures $300 \leq T \leq 1200$ K [35]. In order to determine the most essential parameters that characterize the mechanical response of the studied systems, we here exploit the stress/strain relationships evaluated in the elastic regime [35] to extract the second-order elastic constants (SOEC) of B1 TiC, ZrC, HfC, VC, and TaC, as well as high-entropy (Ti,Zr,Hf,Ta,W)C and (V,Nb,Ta,Mo,W)C. The fact that our approach utilizes six different deformation pathways (see **Section 2.1**) provides SOEC with reduced numerical dependence on the specific choice of strain matrixes and strain intervals [4]. For the two high-entropy carbides (HEC), synthesized as single-phase B1 materials [36-38], we also evaluate the room-temperature elastic moduli from sound velocity measurements that allow us to verify the reliability of AIMD results. We note that the (Ti,Zr,Hf,Ta,W)C system exhibits particularly high hardness [36], while (V,Nb,Ta,Mo,W)C is of interest because of its relatively high valence electron concentration, which may improve ductility [9, 39].

2. Methods

2.1. AIMD simulations

In this work, we employ tensile and shear stress/strain data within the elastic (prior to yielding) material's responses obtained from AIMD simulations performed at $T = 300, 600, 900,$ and 1200 K [40] and evaluate the SOEC of B1 TMC as a function of temperature (T). The entire (elastic and plastic) stress vs. strain curves calculated for TMC subject to tensile and shear deformation will be reported elsewhere [35]. The procedure for AIMD stress/strain calculations is detailed in Refs. [32-34]. The B1 TMC supercells used in our simulations have three different crystallographic orientations (**Fig. 1**), which are convenient for modeling elongation orthogonal to (001), (110), and (111) (i.e., surface terminations of lowest formation energies [41]) and shearing on the primary slip systems of B1-structure ceramics, namely, $\{001\}\{1\bar{1}0\}$, $\{110\}\{1\bar{1}0\}$, and $\{111\}\{1\bar{1}0\}$ [42-45]. The stress vs. strain relationships are fitted with 2nd-order polynomials. Then, the second-order elastic response of the crystal is calculated from the slope of the polynomial in the limit of vanishingly small strain. The approach is analogous to fitting the energy-density vs. strain curves with 3rd-order polynomials, as illustrated, for example, in Ref. [4].

AIMD simulations are carried out with VASP code [46], which implements the projector augmented-wave method [47]. The Perdew-Burke-Ernzerhof (PBE) electronic exchange and correlation functionals of the generalized gradient approximation (GGA) [48], Γ -point sampling of the Brillouin zone, and planewave cutoff energy of 300 eV are used in all simulations. The ionic equations of motion are integrated at timesteps of 1 fs, using 10^{-5} eV/supercell convergence criteria for the total energy during both system equilibration and mechanical testing. Prior to modeling tensile and shear deformation, the supercell equilibrium structural parameters are optimized at each investigated temperature via an iterative NPT [49] simulation procedure, which employs the Parrinello-Rahman barostat [50] and the Langevin thermostat [51]. Subsequently, NVT [52] sampling of the configurational space is used to equilibrate the unstrained structures for 3–5 additional ps using the Nosé-Hoover thermostat [51]. In these simulations, we ensure that the time-averaged $|\sigma_{xx}|, |\sigma_{yy}|,$

and $|\sigma_{zz}|$ stress components are $\lesssim 0.3$ GPa. The structural parameters determined for unstrained (equilibrium) supercells at different temperatures allow us to evaluate lattice constants and average linear thermal expansion coefficients of B1 TMC.

$\langle 001 \rangle$, $\langle 110 \rangle$, $\langle 111 \rangle$ tensile and $\{001\}\langle 1\bar{1}0 \rangle$, $\{110\}\langle 1\bar{1}0 \rangle$, and $\{111\}\langle 1\bar{1}0 \rangle$ shear deformations of B1 stoichiometric TMC are increased at sequential increments of strain $\delta=2\%$, see details in Refs. [32-34]. At each strain, the crystals are equilibrated for (at least) two ps via canonical sampling. All simulation structures contain 576 atoms: 24 atomic layers with 24 atoms per layer. In HEC, the metals are stochastically distributed on the cation sublattice. The values of total stress (including kinetic contributions) values that we report are averaged over 500 equilibrated AIMD configurations.

2.2 Determination of SOEC from AIMD

The six different deformations [three tensile: $\langle 001 \rangle$, $\langle 110 \rangle$, and $\langle 111 \rangle$, with supercell elongation in the vertical z direction; three shearing: $\{001\}\langle 1\bar{1}0 \rangle$, $\{110\}\langle 1\bar{1}0 \rangle$, and $\{111\}\langle 1\bar{1}0 \rangle$ with trigonal strain of supercells within the xz plane (see supercells in **Fig. 1**)] employed in our AIMD simulations, result in 36 independent stress values for each applied tensile or shear strain (δ). δ is the strain increment in either deformation. Of these, thirteen stress components – namely $\sigma_{xx}^{\langle 001 \rangle}$, $\sigma_{yy}^{\langle 001 \rangle}$, $\sigma_{zz}^{\langle 001 \rangle}$, $\sigma_{xx}^{\langle 110 \rangle}$, $\sigma_{yy}^{\langle 110 \rangle}$, $\sigma_{zz}^{\langle 110 \rangle}$, $\sigma_{xx}^{\langle 111 \rangle}$, $\sigma_{yy}^{\langle 111 \rangle}$, $\sigma_{zz}^{\langle 111 \rangle}$, $\sigma_{xz}^{\{001\}\langle 1\bar{1}0 \rangle}$, $\sigma_{xz}^{\{110\}\langle 1\bar{1}0 \rangle}$, $\sigma_{xy}^{\{111\}\langle 1\bar{1}0 \rangle}$, and $\sigma_{xz}^{\{111\}\langle 1\bar{1}0 \rangle}$ – are of relevance to our analysis because their derivative $\left[\frac{\partial \sigma}{\partial \delta} \right]_{\delta=0}$ corresponds to a linear combination of elastic constants [53]. Least-squares fitting is used to determine 2nd order polynomials which best describe the dependences of each of the stress components listed above as a function of δ . The polynomial's first derivatives at 0 strain are gathered in a vector. Then, the canonical elastic stiffness tensor C_{ij} is transformed into the coordinate systems of our supercells (see **Fig. 1**). The elastic constant combinations corresponding to the stresses employed in our analysis are summarized in **Table 1**. The thirteen stress vs. strain relationships define a set of linear equations, which can be written in a matrix expression:

$$\begin{pmatrix}
0 & 1 & 0 \\
0 & 1 & 0 \\
1 & 0 & 0 \\
1/2 & 1/2 & -1 \\
0 & 1 & 0 \\
1/2 & 1/2 & 1 \\
1/3 & 2/3 & -2/3 \\
1/3 & 2/3 & -2/3 \\
1/3 & 2/3 & 4/3 \\
0 & 0 & 1 \\
1/2 & -1/2 & 0 \\
\sqrt{2}/6 & -\sqrt{2}/6 & -\sqrt{2}/3 \\
1/3 & -1/3 & 1/3
\end{pmatrix}
\begin{pmatrix}
C_{11} \\
C_{12} \\
C_{44}
\end{pmatrix}
=
\left[\frac{\partial}{\partial \delta} \right]_{\delta=0}
\begin{pmatrix}
\sigma_{xx}^{\langle 001 \rangle} \\
\sigma_{yy}^{\langle 001 \rangle} \\
\sigma_{zz}^{\langle 001 \rangle} \\
\sigma_{xx}^{\langle 110 \rangle} \\
\sigma_{yy}^{\langle 110 \rangle} \\
\sigma_{zz}^{\langle 110 \rangle} \\
\sigma_{xx}^{\langle 111 \rangle} \\
\sigma_{yy}^{\langle 111 \rangle} \\
\sigma_{zz}^{\langle 111 \rangle} \\
\sigma_{xz}^{\{001\}\langle 1\bar{1}0 \rangle} \\
\sigma_{xz}^{\{110\}\langle 1\bar{1}0 \rangle} \\
\sigma_{xy}^{\{111\}\langle 1\bar{1}0 \rangle} \\
\sigma_{xz}^{\{111\}\langle 1\bar{1}0 \rangle}
\end{pmatrix}. \quad (1)$$

Finally, the cubic SOEC can be derived by solving the overdetermined system of equations (**Eq. (1)**) by a least square fitting approach (multiple linear regression). The procedure allows us reducing the numerical uncertainties in calculated SOEC values due to a specific choice of strain matrix or strain range [4].

The elastic constants C_{11} , C_{12} , C_{44} obtained from **Eq. (1)** are used to compute other elastic properties. Specifically, we derive bulk moduli B , polycrystalline shear G and Young's E moduli according to the Voigt (G_V and E_V), Reuss (G_R and E_R), and Hill (G_H and E_H) approximations (formulas in [30]), directional Young's moduli E_{001} , E_{110} , and E_{111} (expressions in [54]), and elastic shear resistances $G_{110} = (C_{11}-C_{12})/2$, $G_{111u} = (C_{11}+C_{12}+C_{44})/3$, and $G_{111r} = 3C_{44}(C_{11}-C_{12})/(4C_{44}+C_{11}+C_{12})$ resolved onto $\{110\}\langle 1\bar{1}0 \rangle$ and $\{111\}\langle 1\bar{1}0 \rangle$ slip systems. The subscripts u and r are used to label unrelaxed (constant strain) and relaxed (constant stress) G_{111} shear moduli. In this work, we focus on the G_{111u} rather than G_{111r} moduli, because our simulations are performed with constant strain boundary conditions. The Poisson's ratios ν are computed as $\nu = 1/2 [1-E_H/(3B)]$.

2.3 Material synthesis and elastic constants measurements

For fabricating the high entropy carbides used in this study, binary carbide powders were weighted out in 24 gram quantities to achieve an equiatomic mixture of the 5 metallic species,

additional graphite was added to yield the stoichiometric monocarbide ratios when Mo₂C was included. The binary carbides included: TiC, ZrC, HfC, VC, TaC, Mo₂C and WC, all obtained from Alfa Aesar, USA. The powders were blended and hand mixed to achieve the following bulk compositions: (Ti,Zr,Hf,Ta,W)C and (V,Nb,Ta,Mo,W)C, followed by high energy ball milling in 30 minute increments, for a total of 120 minutes, using 10-minute cooling periods between each step. The powder samples were then compacted and sintered using current and pressure assisted densification (CAPAD) in a well-controlled vacuum environment. The samples were sintered using 20mm diameter graphite dies and plungers. The initial vacuum condition was 20 mTorr, and upon heating, whenever the vacuum decreased to 100 mTorr, the heating profile was paused to allow the vacuum to return to the 20 mTorr level. The heating and pressure profile used in the sintering of both materials was as follows: using an initial pressure of 5 MPa, the samples were heated at 100°C per minute to 2200°C, then held at temperature for 9 minutes, before increasing the pressure to 80 MPa over one minute, then holding at this pressure and 2200°C for 15 minutes. The samples were subsequently cooled to room temperature in vacuum under 5 MPa pressure. Each sample was ground on both circular faces to remove any excess graphite from the die setup, then polished using standard metallurgical techniques to a final polish of 0.04 μm colloidal silica. The carbon-to-metal ratios assessed for our HEC specimens are 0.90±0.03 [55].

To obtain the elastic moduli, both longitudinal and shear, the method outlines in ASTM E494-15 (Standard Practice for Measuring Ultrasonic Velocity in Materials) were followed, using the 20 mm diameter and ~3 mm thick sintered high entropy carbide samples. The samples were placed on an acoustically-isolated substrate for wave speed measurements using separate piezoelectric transducers for longitudinal and shear velocities. A total of 4 separate measurements, in each velocity direction, were obtained in order to compute the respective wave speeds from which to compute the different elastic properties. To compute the various elastic constants, both the respective wave speeds and the sample density must be measured, with the latter measured by Archimedes method. The following equations were used to compute the elastic properties, which assume isotropic elastic

responses. For Poisson's ratio: $\nu = (V_L^2 - 2V_S^2)/[2(V_L^2 - V_S^2)]$; for Young's modulus: $E = 2 V_S^2 \rho (1 + \nu)$; for shear modulus: $G = V_S^2 \rho$; and for bulk modulus: $B = E/[3(1-2\nu)]$, where ρ is density, V_L is the measured longitudinal wave speed and V_S is the measured shear wave speed.

3. Results and discussion

The calculated and experimental lattice parameters and average linear thermal expansion coefficients α of B1 TiC, ZrC, HfC, VC, TaC, (Ti,Zr,Hf,Ta,W)C, and (V,Nb,Ta,Mo,W)C at temperatures ranging from 0 to 1200 K are presented in **Table 2 (AIMD data listed in bold)**. Previous 0-K *ab initio* calculations based on GGA slightly overestimate (by less than 1%) the experimental lattice parameters of B1 TMC (see **Table 2**). The discrepancy is due to known limitations of GGA functionals [56], as well as to the fact that the synthesized transition-metal carbides typically contain anion vacancies, which reduce equilibrium volumes [57, 58]. At deviance with *ab initio* results at 0 K, our AIMD simulations yield lattice constants that are systematically $\approx 0.5\%$ smaller than experimental values measured at 300 K. This is likely due to the relatively lower accuracy of present simulations (details in **Section 2.1**) in comparison with static *ab initio* calculations, for which the structural parameters are converged with respect to cutoff energies and k-point mesh thicknesses at low computational efforts. Overall, our AIMD results closely match with the lattice constants and thermal expansion coefficients determined by experiments at different temperatures (**Table 2**).

The SOEC of refractory carbides, nitrides, and borides have been extensively investigated via first-principles energy-minimization methods at 0 kelvin [4, 16-18, 23, 59-61]. In contrast, information concerning finite-temperature elastic properties is rather sparse for these classes of materials. Finite-temperature estimations of SOEC can be efficiently obtained using static *ab initio* calculations that employ the quasiharmonic approximation (QHA) [23, 27, 62] or volume-scaling methods [28, 31]. These methods account for lattice thermal expansion while neglect anharmonic vibrational effects. The latter effects can yield significant corrections to SOEC values calculated at

high temperatures using static *ab initio* approaches, as demonstrated for the cases of B1 TiN, CrN, and (Ti,Al)N compounds [28, 31]. A more detailed comparison among AIMD, static *ab initio*, and experimental results of elastic properties as a function of temperature can be found below, toward the end of **Section 3**.

To the authors' knowledge, very few studies based on AIMD simulations – which inherently describe lattice vibrations – focused on direct evaluation of the elastic properties of refractory ceramics [30-33, 63]. The elastic properties of B1 TiC, ZrC, HfC, VC, TaC, (Ti,Zr,Hf,Ta,W)C, and (V,Nb,Ta,Mo,W)C determined by AIMD simulations between 300 and 1200 K are listed in **bold in Tables 3–9**. For comparison, the tables also contain data reported in other theoretical and experimental works. Previous studies mainly focused on synthesis and investigation of group-IV carbides. Measurements and *ab initio* results for the properties of VC and TaC are sparser. In addition, the information available for the B1 carbides of vanadium and tantalum show considerable incongruences. For example, the Young's moduli measured at 300 K are scattered in the range 268 – 420 GPa for vanadium carbides and 241 – 722 GPa for tantalum carbides [36]. To some extent, such large deviations can be attributed to variations in metal/carbon stoichiometries and different porosity of the samples. In the case of HEC, a new class of refractory ceramics, the information available in the literature is limited to properties calculated at 0 K or determined by experiments at room temperature [36, 37].

Overall, our AIMD results closely match with experimental [64] and *ab initio* values retrievable from the literature (**Tables 3–9**). For example, the temperature dependence of the Young's moduli E of B1 zirconium carbides, previously determined by experiments [65-67] and other *ab initio* calculations based on the QHA [27], agrees with the results of AIMD simulations (**Table 4**). The variation of E vs. T shows that the elastic modulus of ZrC decreases at a quasi-linear decay rate $(1/E_{300K}) \times (dE/dT) \approx -1.1 \pm 0.2 \times 10^{-4} \text{ K}^{-1}$ for temperatures increasing from 300 to 1200 K. Note that the decay coefficient varies with the sample stoichiometry [67]. A decrease in elastic stiffness vs. T is expected for crystal phases that are dynamically stable from 0 K to melting points. The monotonic

reduction in SOEC with increasing temperature [68-70] is also reflected by a corresponding decrease in mechanical strength and hardness [42, 71]. Deviations from the typical behavior of SOEC vs. T – see, e.g., temperature-induced increase in the C_{44} of some metals [72, 73] – may arise from strain- or thermally-induced modifications of electronic-structures.

All TMC modelled in this work display expected trends in C_{11} and C_{44} vs. temperature. Both elastic constants decrease monotonically from 300 to 1200 K (**Fig. 2a and 2c**). Conversely, the values of the C_{12} elastic constants appear to be less affected by temperature. Indeed, the C_{12} calculated for TaC, HfC, and (Ti,Zr,Hf,Ta,W)C remains nearly unvaried (within statistical uncertainty) with T (**Fig. 2b**). The trends that we obtain for all other carbides indicate slow C_{12} reductions with increasing temperature (**Fig. 2b**). The diminution in C_{11} and C_{44} implies that the moduli B, G, and E decrease as a function of temperature for all materials considered here (**Fig. 2e-f**).

Consistent with the temperature dependence observed for the polycrystalline moduli G and E, the directional elastic E_{001} , E_{110} , E_{111} and shear G_{001} , G_{110} , G_{111u} moduli of the investigated carbide systems decrease with increasing T (**Figs. 2c, 3a-e**). The moduli E_{hkl} and G_{hkl} of each material strictly maintain a mutual relationship [$E_{001} > E_{110} > E_{111}$] and [$G_{110} > G_{111u} > G_{001} (\equiv C_{44})$] from 300 and up to 1200 K. This can be seen by gathering E_{hkl} and G_{hkl} data from **Figs. 2c, 3a-e**. Given that $E_{001} > E_{110} > E_{111}$, it is concluded that the TMC systems retain similar directionality in bond stiffnesses at all investigated temperatures; this is also reflected by the calculated trends in coefficients A (**Tables 3–9**) which, overall, indicate a modest increase in TMC elastic isotropy between 300 and 1200 K.

The fact that G_{110} – elastic resistance to $\{110\}$ plane shearing along $\langle 1\bar{1}0 \rangle$ – and G_{001} – elastic resistance to $\{001\}$ plane shearing along $\langle 1\bar{1}0 \rangle$ – are systematically the highest and lowest shear moduli may (naively) appear inconsistent with experimental findings for plastic deformation mechanisms in B1 carbides. In this regard, several experimental studies showed that $\{110\}\langle 1\bar{1}0 \rangle$ slip is the most active in transition metal carbides at low temperature, whereas lattice slip on $\{111\}$ planes becomes generally operative at moderate or high temperatures [42, 43, 74]. In contrast, $\{001\}\langle 1\bar{1}0 \rangle$ glide in carbides has been experimentally observed in very few cases [44, 45]. Nonetheless, a stiffer

elastic response to change of shape (quantified by the shear moduli) does not necessarily imply that the shear strength (resistance to slip) is larger. For example, B1 VN_{0.8} exhibits greater elastic shear stiffness, but much lower shear strength than B1 VN [32]. Analogously, although TaC displays the highest shear moduli G_{111u} among all TMC (**Fig. 3b**), $\{111\}\langle 1\bar{1}0\rangle$ plastic deformation of B1 TaC crystals can be observed already at room temperature [74].

At relatively low temperatures, mechanical strength and plastic deformation in B1-structure ceramics is primarily controlled by dislocation mobilities [43-45, 74]. The mobility is, in turn, dictated by the core structure of the line defect. An atomic-level determination of dislocation core structures in ceramics can be a formidable task. The problem is further complicated by the fact that dislocation cores may exhibit different polymorph variants [75, 76] and be affected by lattice stoichiometry [77]. For these reasons, several empirical criteria have been proposed for rapidly predicting qualitative trends in ductility and strength among different materials. For example, the criterion proposed by Pugh [12] has a broad applicability because it bases its predictions on the ratio between polycrystalline moduli G and B . Pettifor's criterion [13], on another hand, is useful to estimate trends in ductility among crystals with cubic symmetry. Remarkably, the use of these phenomenological criteria [9, 17] has led to the discovery of hard and inherently tough ceramics [10].

Recently, a generalization of Pugh's and Pettifor's criteria [7], in which the Cauchy's pressure $C_{12}-C_{44}$ is normalized with the modulus E , has been proposed for reproducing experimental trends in ductility vs. strength across different classes of solids. The empirical criterion of Niu *et al.* [7] suggests that strength and ductility are necessarily mutually exclusive properties in crystals: high G/B (high strength) implies low $(C_{12}-C_{44})/E$ (poor ductility \equiv brittleness), and vice-versa. The map in ductility vs. strength determined for B1 TMC is illustrated in **Fig. 3f**, where G/B vs. $(C_{12}-C_{44})/E$ are plotted for each investigated temperature. The AIMD results in **Tables 3, 4, 5, and 8** show that the G/B and $(C_{12}-C_{44})/E$ values calculated for the three Group-IVB carbides, as well as B1 (Ti,Zr,Hf,Ta,W)C, remain approximately constant with temperature. We note that B1 HfC is the crystal phase characterized by the highest G/B values, and lowest $(C_{12}-C_{44})/E$, from 300 to 1200 K

(**Fig. 3f**). Conversely, B1 VC, TaC, and (V,Nb,Ta,Mo,W)C are predicted to become more ductile (and less strong) with increasing temperature (see arrow in **Fig. 3f**).

Previous *ab initio* studies conducted on refractory B1-structure ceramics indicated that an increased valence electron concentration (VEC) enhances the material's ductility [9, 16-18]. Overall, the trends illustrated in **Fig. 3f** are aligned with such empirical rule. Indeed, a plot of $[G/B]_{\text{VEC}}$ vs. $[(C_{12}-C_{44})/E]_{\text{VEC}}$ – where “[...]” denotes a property-average for an isoelectronic class of TMC – predicts that Group-IVB carbides (VEC=8.0 e⁻/f.u.) are the strongest, but also the most brittle systems, whereas (V,Nb,Ta,Mo,W)C (VEC=9.4 e⁻/f.u.) is the material which, by far, exhibits the best ductility (inset in **Fig. 3f**). The strength G/B and ductility (C₁₂–C₄₄)/E indicators calculated for the high entropy (Ti,Zr,Hf,Ta,W)C system are intermediate to the values obtained for binary Group-IVB and Group-VB TMC (inset in **Fig. 3f**). This is consistent with the VEC rule, because the HEC's electron concentration (8.6 e⁻/f.u.) is between those of Group-IVB (8.0 e⁻/f.u.) and Group-VB (9.0 e⁻/f.u.) carbides.

The theoretical prediction that TaC and VC should be more ductile than TiC, ZrC, and HfC is consistent with the fact that {111}{1 $\bar{1}$ 0} slip in Group-VB carbides is activated at lower temperatures than in Group-IVB carbides [42]. The operativity of lattice slip on {111} crystallographic planes is of crucial importance for ductility in B1-structure ceramics, because it provides a sufficient number of independent pathways to induce plastic deformation [78]. In agreement with the conclusions of Ref. [42], other experiments have shown that the concentration of intrinsic {111} stacking faults in B1 TaC is much greater than in, e.g., B1 HfC [79]. The observation has been rationalized by *ab initio* results, which indicated that these extended defects are metastable in Group-VB, whereas they are unstable in Group-IVB carbides (see [79] with supplemental material). The energetically-favored formation of {111} stacking faults facilitates, in turn, plastic deformation via {111}{11 $\bar{2}$ } synchro-shear mechanisms [79].

The results of our AIMD simulations demonstrate that TaC is the system of highest elastic resistances to tensile (C₁₁, E, E₀₀₁, E₁₁₀, E₁₁₁) as well as shear (C₄₄, G, G₁₁₀, G_{111u}) deformation at all

investigated temperatures, **Figs. 2 and 3**. VC is the crystal with second highest tensile and shear elastic stiffnesses (with a few exceptions for $T \approx 1200$ K). Conversely, we find that B1 ZrC generally displays the lowest values of G and E elastic stiffnesses. With regard to high entropy alloys, **Fig. 2a** shows that the C_{11} elastic constants of $(\text{Ti,Zr,Hf,Ta,W})\text{C}$ and $(\text{V,Nb,Ta,Mo,W})\text{C}$ are nearly identical, and with values intermediate to those of Group-IV and Group-V carbides at the temperatures probed in the present work. Our AIMD results also demonstrate that $(\text{V,Nb,Ta,Mo,W})\text{C}$ possesses the lowest C_{44} and highest C_{12} values for $300 \leq T \leq 1200$ K (**Fig. 2c**). As discussed above and illustrated in **Fig. 3f**, this is reflected by its highest predicted ductility (empirical indicator $(C_{12}-C_{44})/E$ [7]).

Among numerous multicomponent carbide alloys synthesized during recent years [36-38, 80-83], here we focus on B1 $(\text{Ti,Zr,Hf,Ta,W})\text{C}$ and B1 $(\text{V,Nb,Ta,Mo,W})\text{C}$ due to expectations for particularly high hardness and toughness, respectively. The VEC ($8.6 e^-/\text{f.u.}$) of $(\text{Ti,Zr,Hf,Ta,W})\text{C}$ is close to the value ($\approx 8.4 e^-/\text{f.u.}$) that maximizes hardness in B1-structure carbonitrides [5]. The electronic mechanism for increased hardness in the single-crystal B1 phase finds its origin in fully occupied shear-resistant metal(d)-non-metal(p) vs. empty shear-sensitive metal(d)-metal(d) electronic states. In the case of $(\text{V,Nb,Ta,Mo,W})\text{C}$ ($9.4 e^-/\text{f.u.}$), we envisage an energetically-favored formation of $\{111\}$ stacking faults (during synthesis or upon loading), as previously demonstrated for B1-structure carbides and nitrides of similar VEC ($\approx 9.5 e^-/\text{f.u.}$). [84, 85]. Hindered dislocation motion across the faults provides high hardness and mechanical strength [84, 85]. $(\text{V,Nb,Ta,Mo,W})\text{C}$ does indeed exhibit rather high hardness values (27 ± 3 GPa [37]). Concurrently, a substantial amount of Mo and W in the host B1 $(\text{V,Nb,Ta,Mo,W})\text{C}$ lattice should promote slip on $\{111\}$ lattice planes [86], which fulfills the criteria for plasticity in B1-structure crystals [78]. $\{111\}\langle 11\bar{2}\rangle$ synchro-shear, activated upon loading in alloy domains characterized by locally higher concentrations of Group-VIB metals, produces $\{111\}$ stacking faults or twins in the B1 lattice (note that near-stoichiometric MoC_x and WC_x are thermodynamically-inclined to form the hexagonal WC structure [87, 88] with A-B-A-B stacking sequence along $[0001]$). Relatively facile $\{111\}\langle 11\bar{2}\rangle$ deformation provides a transformation pathway for stress dissipation and thus enhances toughness.

The elastic moduli of the two HEC systems investigated in this work have been previously assessed by experiments and *ab initio* calculations [36]. Our AIMD results for B, G, E, and ν of the HECs at 300 K closely match (deviations $< 5\%$) with first-principles elastic properties at 0 K [36] and are also in good agreement with previous experimental data [36] (see **Tables 8 and 9**). Our present measurements of acoustic wave speeds in the HECs return elastic stiffnesses and Poisson's ratios (see **(values)** in **Tables 8 and 9**) that are in quantitative agreement with AIMD predictions. Our AIMD vs. (experimental) results are (i) bulk moduli $B^{(\text{Ti,Zr,Hf,Ta,W})\text{C}} = 288$ (273 ± 17) GPa, $B^{(\text{V,Nb,Ta,Mo,W})\text{C}} = 311$ (269 ± 12) GPa; (ii) shear moduli $G^{(\text{Ti,Zr,Hf,Ta,W})\text{C}} = 194$ (193 ± 4) GPa, $G^{(\text{V,Nb,Ta,Mo,W})\text{C}} = 174$ (173 ± 4) GPa; (iii) Young's moduli $E^{(\text{Ti,Zr,Hf,Ta,W})\text{C}} = 475$ (468 ± 3) GPa, $E^{(\text{V,Nb,Ta,Mo,W})\text{C}} = 440$ (426 ± 5) GPa; (iv) Poisson's ratios $\nu^{(\text{Ti,Zr,Hf,Ta,W})\text{C}} = 22$ (21 ± 2) %, $\nu^{(\text{V,Nb,Ta,Mo,W})\text{C}} = 26$ (24 ± 1) %.

Before conclusions, we offer a comparison of different computational techniques for the evaluation of finite-temperature elastic properties. As anticipated at the beginning of this section, finite-temperature elastic properties of some refractory nitrides and carbides have been calculated via the QHA [23, 27, 62] or volume-scaling methods [28, 31] in the framework of *static* first-principles techniques. These, however, generally produce a slower decay in elastic stiffnesses vs. T than methods which account for intrinsic anharmonic effects, as demonstrated for B1 $\text{Ti}_{1-x}\text{Al}_x\text{N}$ [28] and CrN [31] refractory compounds. Here we extend the analyses of Refs. [28, 31] by showing trends in elastic constants vs. T obtained by AIMD simulations, experiments, and static *ab initio* calculations.

Fig. 4 illustrates the temperature dependences of the elastic shear stiffnesses of (a) TiC, (b) ZrC, and (c) TiN. Note that B1 TiN is included in our analysis because of the sparseness of temperature-dependent elastic properties for refractory carbides. A detailed description of the elastic properties of TiN and other nitrides will be provided elsewhere [35]. In all three cases presented in **Fig. 4**, one can see that the explicit treatment of lattice vibrations – inherent to AIMD simulations – yields a decrease of shear-stiffness vs. T in closer agreement with experimental trends. Conversely, static *ab initio* and AIMD results of other elastic properties are in apparently similar agreement with

experimental trends (compare, e.g., C_{11} and C_{12} vs. T for TiC, **Table 3**, and B and E vs. T for ZrC, **Table 4**). This suggests that the inclusion of vibrational effects is of particular importance to achieve accurate temperature-dependent elastic shear stiffnesses C_{44} , which, in turn, strongly affect the values of polycrystalline shear moduli G .

4. Conclusions

We employ AIMD simulations and sound velocity measurements to provide an accurate database of elastic properties of B1-structure refractory compound and multicomponent carbides from 300 to 1200 K. Exception made for the C_{12} , our results show that the elastic constants of all carbides decrease monotonically with increasing temperature. B1 TaC is the material which displays the highest values of C_{11} , C_{44} , B , G , and E moduli up to 1200 K. A comparison of the results of present AIMD simulations, previous static *ab initio* calculations, and experiments suggests that the explicit treatment of lattice vibrations is necessary to achieve qualitatively correct trends in C_{44} vs. T . Based on empirical criteria used to assess ductility trends and previous hardness measurements ($H \approx 27$ GPa), we propose the high-entropy (V,Nb,Ta,Mo,W)C ceramic as candidate carbide system with high toughness both at room and elevated temperature.

Acknowledgements

All simulations were carried out using the resources provided by the Swedish National Infrastructure for Computing (SNIC) – partially funded by the Swedish Research Council through Grant Agreement N° VR-2015-04630 – on the Clusters located at the National Supercomputer Centre (NSC) in Linköping, the Center for High Performance Computing (PDC) in Stockholm, and at the High Performance Computing Center North (HPC2N) in Umeå, Sweden. We gratefully acknowledge financial support from the Competence Center Functional Nanoscale Materials (FunMat-II) (Vinnova Grant No. 2016–05156), the Swedish Research Council (VR) through Grant No. 2019–05600, the Swedish Government Strategic Research Area in Materials Science on Functional Materials at Linköping University (Faculty Grant SFO-Mat-LiU No. 2009-00971), and the Knut and Alice Wallenberg Foundation through Wallenberg Scholar project (Grant No. 2018.0194). D.G.S. gratefully acknowledges financial support from the Olle Engkvist Foundation. TH and KV would like to acknowledge support through the Office of Naval Research ONR-MURI (grant No. N00014-15-1-2863). Analysis of results of theoretical simulations was supported by RFBR Project N° 20-02-00178.

References

- [1] F. Mouhat, F.X. Coudert, Necessary and sufficient elastic stability conditions in various crystal systems, *Physical Review B* 90 (2014) 224104.
- [2] M.P.J. Joesaar, N. Norrby, J. Ullbrand, R. M'Saoubi, M. Oden, Anisotropy effects on microstructure and properties in decomposed arc evaporated $Ti_{1-x}Al_xN$ coatings during metal cutting, *Surface & Coatings Technology* 235 (2013) 181.
- [3] A. Horling, L. Hultman, M. Oden, J. Sjolen, L. Karlsson, Thermal stability of arc evaporated high aluminum-content $Ti_{1-x}Al_xN$ thin films, *Journal of Vacuum Science & Technology A* 20 (2002) 1815.
- [4] D. Holec, M. Friak, J. Neugebauer, P.H. Mayrhofer, Trends in the elastic response of binary early transition metal nitrides, *Physical Review B* 85 (2012) 064101.
- [5] S.H. Jhi, J. Ihm, S.G. Louie, M.L. Cohen, Electronic mechanism of hardness enhancement in transition-metal carbonitrides, *Nature* 399 (1999) 132.
- [6] Y. Tian, B. Xu, Z. Zhao, Microscopic theory of hardness and design of novel superhard crystals, *International Journal of Refractory Metals & Hard Materials* 33 (2012) 93.
- [7] H.Y. Niu, X.Q. Chen, P.T. Liu, W.W. Xing, X.Y. Cheng, D.Z. Li, Y.Y. Li, Extra-electron induced covalent strengthening and generalization of intrinsic ductile-to-brittle criterion, *Scientific Reports* 2 (2012) 718.
- [8] M. de Jong, I. Winter, D.C. Chrzan, M. Asta, Ideal strength and ductility in metals from second- and third-order elastic constants, *Physical Review B* 96 (2017) 014105.
- [9] D.G. Sangiovanni, L. Hultman, V. Chirita, Supertoughening in B1 transition metal nitride alloys by increased valence electron concentration, *Acta Materialia* 59 (2011) 2121.
- [10] H. Kindlund, D.G. Sangiovanni, L. Martinez-De-Olcoz, J. Lu, J. Jensen, J. Birch, I. Petrov, J.E. Greene, V. Chirita, L. Hultman, Toughness enhancement in hard ceramic thin films by alloy design, *APL Materials* 1 (2013) 042104.
- [11] H.Y. Niu, S.W. Niu, A.R. Oganov, Simple and accurate model of fracture toughness of solids, *Journal of Applied Physics* 125 (2019) 065105.
- [12] S.F. Pugh, Relations between the elastic moduli and the plastic properties of polycrystalline pure metals, *Philosophical Magazine* 45 (1954) 823.
- [13] D.G. Pettifor, Theoretical predictions of structure and related properties of intermetallics, *Materials Science and Technology* 8 (1992) 345.
- [14] M. de Jong, W. Chen, T. Angsten, A. Jain, R. Notestine, A. Gamst, M. Sluiter, C.K. Ande, S. van der Zwaag, J.J. Plata, C. Toher, S. Curtarolo, G. Ceder, K.A. Persson, M. Asta, Charting the complete elastic properties of inorganic crystalline compounds, *Scientific Data* 2 (2015) 150009.
- [15] Y. Gao, C.J. Ruestes, H.M. Urbassek, Nanoindentation and nanoscratching of iron: Atomistic simulation of dislocation generation and reactions, *Computational Materials Science* 90 (2014) 232.
- [16] K. Balasubramanian, S.V. Khare, D. Gall, Valence electron concentration as an indicator for mechanical properties in rocksalt structure nitrides, carbides and carbonitrides, *Acta Materialia* 152 (2018) 175.
- [17] D. Edström, D.G. Sangiovanni, L. Hultman, V. Chirita, Effects of atomic ordering on the elastic properties of TiN- and VN-based ternary alloys, *Thin Solid Films* 571 (2014) 145.
- [18] D.G. Sangiovanni, V. Chirita, L. Hultman, Toughness enhancement in TiAlN-based quaternary alloys, *Thin Solid Films* 520 (2012) 4080.
- [19] G. Abadias, P. Djemia, L. Belliard, Alloying effects on the structure and elastic properties of hard coatings based on ternary transition metal (M = Ti, Zr or Ta) nitrides, *Surface & Coatings Technology* 257 (2014) 129.
- [20] E. Mazhnik, A.R. Oganov, Application of machine learning methods for predicting new superhard materials, *Journal of Applied Physics* 128 (2020) 075102.
- [21] W. Sun, C.J. Bartel, E. Arca, S.R. Bauers, B. Matthews, B. Orvananos, B.-R. Chen, M.F. Toney, L.T. Schelhas, W. Tumas, J. Tate, A. Zakutayev, S. Lany, A.M. Holder, G. Ceder, A map of the inorganic ternary metal nitrides, *Nature Materials* 18 (2019) 732.

- [22] P. Avery, X. Wang, C. Oses, E. Gossett, D.M. Proserpio, C. Toher, S. Curtarolo, E. Zurek, Predicting superhard materials via a machine learning informed evolutionary structure search, *npj Computational Materials* 5 (2019) 89.
- [23] D.Y. Dang, J.L. Fan, H.R. Gong, Thermodynamic and mechanical properties of TiC from *ab initio* calculation, *Journal of Applied Physics* 116 (2014) 033509.
- [24] J. Kim, Y.J. Suh, Temperature dependent elastic and thermal expansion properties of W₃Co₃C, W₆Co₆C and W₄Co₂C ternary carbides, *Journal of Alloys and Compounds* 666 (2016) 262.
- [25] A. Wang, S.-L. Shang, M. He, Y. Du, L. Chen, R. Zhang, D. Chen, B. Fan, F. Meng, Z.-K. Liu, Temperature-dependent elastic stiffness constants of fcc-based metal nitrides from first-principles calculations, *Journal of Materials Science* 49 (2014) 424.
- [26] H. Xiang, Z. Feng, Z. Li, Y. Zhou, Theoretical investigations on mechanical and dynamical properties of MAiB (M = Mo, W) nanolaminated borides at ground-states and elevated temperatures, *Journal of Alloys and Compounds* 738 (2018) 461.
- [27] J. Zhang, J.M. McMahon, Temperature-dependent mechanical properties of ZrC and HfC from first principles, arXiv:2002.07903 (2020).
- [28] N. Shulumba, O. Hellman, L. Rogström, Z. Raza, F. Tasnadi, I.A. Abrikosov, M. Oden, Temperature-dependent elastic properties of Ti_{1-x}Al_xN alloys, *Applied Physics Letters* 107 (2015) 231901.
- [29] J. Tidholm, F. Tasnadi, I.A. Abrikosov, Accurate prediction of high-temperature elastic constants of Ti_{0.5}Al_{0.5}N random alloy, (submitted) (2020).
- [30] P. Steneteg, O. Hellman, O.Y. Vekilova, N. Shulumba, F. Tasnadi, I.A. Abrikosov, Temperature dependence of TiN elastic constants from *ab initio* molecular dynamics simulations, *Physical Review B* 87 (2013) 094114.
- [31] E. Mozafari, N. Shulumba, P. Steneteg, B. Alling, I.A. Abrikosov, Finite-temperature elastic constants of paramagnetic materials within the disordered local moment picture from *ab initio* molecular dynamics calculations, *Physical Review B* 94 (2016) 054111.
- [32] A.B. Mei, H. Kindlund, E. Broitman, L. Hultman, I. Petrov, J.E. Greene, D.G. Sangiovanni, Adaptive hard and tough mechanical response in single-crystal B1 VN_x ceramics via control of anion vacancies, *Acta Materialia* 192 (2020) 78.
- [33] D.G. Sangiovanni, F. Tasnadi, L.J.S. Johnson, M. Oden, I.A. Abrikosov, Strength, transformation toughening, and fracture dynamics of rocksalt-structure Ti_{1-x}Al_xN (0 ≤ x ≤ 0.75) alloys, *Physical Review Materials* 4 (2020) 033605.
- [34] D.G. Sangiovanni, Inherent toughness and fracture mechanisms of refractory transition-metal nitrides via density-functional molecular dynamics, *Acta Materialia* 151 (2018) 11.
- [35] D.G. Sangiovanni, I.A. Abrikosov (unpublished).
- [36] P. Sarker, T. Harrington, C. Toher, C. Oses, M. Samiee, J.P. Maria, D.W. Brenner, K.S. Vecchio, S. Curtarolo, High-entropy high-hardness metal carbides discovered by entropy descriptors, *Nature Communications* 9 (2018) 4980.
- [37] T.J. Harrington, J. Gild, P. Sarker, C. Toher, C.M. Rost, O.F. Dippo, C. McElfresh, K. Kaufmann, E. Marin, L. Borowski, P.E. Hopkins, J. Luo, S. Curtarolo, D.W. Brenner, K.S. Vecchio, Phase stability and mechanical properties of novel high entropy transition metal carbides, *Acta Materialia* 166 (2019) 271.
- [38] D.Q. Liu, A.J. Zhang, J.G. Jia, J.H. Meng, B. Su, Phase evolution and properties of (VNbTaMoW)C high entropy carbide prepared by reaction synthesis, *Journal of the European Ceramic Society* 40 (2020) 2746.
- [39] D. Edström, D.G. Sangiovanni, L. Hultman, I. Petrov, J.E. Greene, V. Chirita, Elastic properties and plastic deformation of TiC- and VC-based alloys, *Acta Materialia* 144 (2018) 376.
- [40] See AIMD data in supplemental information.
- [41] W. Liu, X. Liu, W.T. Zheng, Q. Jiang, Surface energies of several ceramics with NaCl structure, *Surface Science* 600 (2006) 257.
- [42] R.H.J. Hannink, D.L. Kohlstedt, M.J. Murray, Slip system determination in cubic carbides by hardness anisotropy, *Proceedings of the Royal Society of London A* 326 (1972) 409.

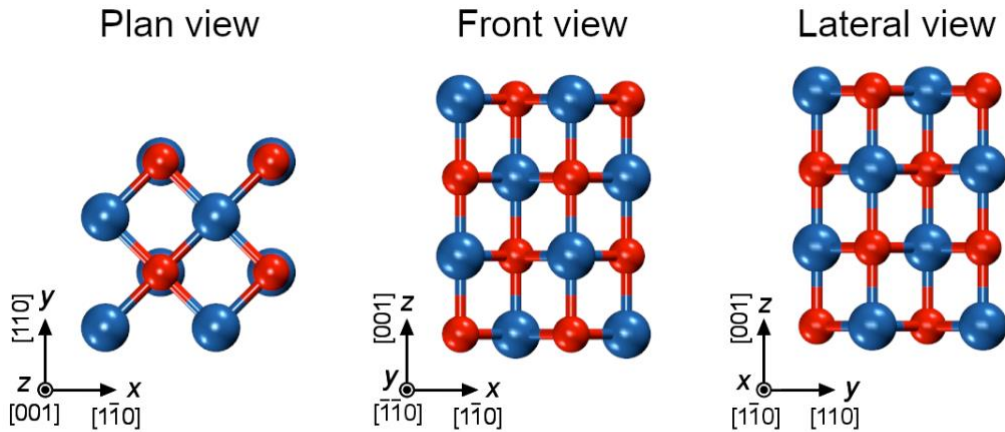
- [43] D.J. Rowcliffe, G.E. Hollox, Hardness anisotropy, deformation mechanisms and brittle-to-ductile transition in carbide, *Journal of Materials Science* 6 (1971) 1270.
- [44] S. Kiani, J.-M. Yang, S. Kodambaka, Nanomechanics of Refractory Transition-Metal Carbides: A Path to Discovering Plasticity in Hard Ceramics, *Journal of the American Ceramic Society* 98 (2015) 2313.
- [45] S. Kiani, C. Ratsch, A.M. Minor, S. Kodambaka, J.M. Yang, Orientation- and size-dependent room-temperature plasticity in ZrC crystals, *Philosophical Magazine* 95 (2015) 985.
- [46] G. Kresse, J. Furthmüller, Efficient iterative schemes for *ab initio* total-energy calculations using a plane-wave basis set, *Physical Review B* 54 (1996) 11169.
- [47] P.E. Blöchl, Projector augmented-wave method, *Physical Review B* 50 (1994) 17953.
- [48] J.P. Perdew, K. Burke, M. Ernzerhof, Generalized gradient approximation made simple, *Physical Review Letters* 77 (1996) 3865.
- [49] NPT ensemble: constant number of particles N, pressure P, and temperature T.
- [50] M. Parrinello, A. Rahman, Polymorphic transitions in single-crystals – a new molecular-dynamics method, *Journal of Applied Physics* 52 (1981) 7182.
- [51] M.P. Allen, D.J. Tildesley, *Computer simulation of liquids*, Oxford University Press (1989).
- [52] NVT ensemble: constant number of particles N, volume V, and temperature T.
- [53] The first derivative in strain of the other 23 stress components is equal zero.
- [54] J.O. Kim, J.D. Achenbach, P.B. Mirkarimi, M. Shinn, S.A. Barnett, Elastic-constants of single-crystal transition-metal nitride films measured by line-focus acoustic microscopy, *Journal of Applied Physics* 72 (1992) 1805.
- [55] K.S. Vecchio, (unpublished).
- [56] A.V. Ruban, I.A. Abrikosov, Configurational thermodynamics of alloys from first principles: effective cluster interactions, *Reports on Progress in Physics* 71 (2008) 046501.
- [57] H.W. Hugosson, P. Korzhavyi, U. Jansson, B. Johansson, O. Eriksson, Phase stabilities and structural relaxations in substoichiometric TiC_{1-x} , *Physical Review B* 63 (2001) 165116
- [58] L. Ramqvist, K. Hamrin, G. Johansson, U. Gelius, C. Nordling, VC, NbC and TaC with varying carbon content studied by ESCA, *Journal of Physics and Chemistry of Solids* 31 (1970) 2669.
- [59] X. Zhang, X. Luo, J. Li, P. Hu, J. Han, The ideal strength of transition metal diborides TMB_2 (TM = Ti, Zr, Hf): Plastic anisotropy and the role of prismatic slip, *Scripta Materialia* 62 (2010) 625.
- [60] G.S. Gautam, K.C.H. Kumar, Elastic, thermochemical and thermophysical properties of rock salt-type transition metal carbides and nitrides: A first principles study, *Journal of Alloys and Compounds* 587 (2014) 380.
- [61] X.-X. Yu, G.B. Thompson, C.R. Weinberger, Influence of carbon vacancy formation on the elastic constants and hardening mechanisms in transition metal carbides, *Journal of the European Ceramic Society* 35 (2015) 95.
- [62] D. Chen, J. Chen, Y. Zhao, B. Yu, C. Wang, D. Shi, Theoretical study of the elastic properties of titanium nitride, *Acta Metallurgica Sinica-English Letters* 22 (2009) 146.
- [63] S.C. Zhang, H. Sun, Effects of boron defects on mechanical strengths of TiB_2 at high temperature: *ab initio* molecular dynamics studies, *Physical Chemistry Chemical Physics* 22 (2020) 6560.
- [64] Note that most experiments are performed on carbon-deficient TMC samples. In some cases, the TMC specimen is also porous. For these reasons, the experimentally measured elastic constants and moduli are typically lower than calculated values.
- [65] R.W. Harrison, W.E. Lee, Processing and properties of ZrC, ZrN and ZrCN ceramics: a review, *Advances in Applied Ceramics* 115 (2016) 294.
- [66] Y.V. Miloserdin, V.M. Baranov, O.S. Korostin, Apparatus for measuring the elastic constants of small samples of isotropic materials at temperatures to 1700° C, *Strength of Materials* 3 (1971) 104.
- [67] V.M. Baranov, V.I. Knyazev, O.S. Korostin, The temperature dependence of the elastic constants of nonstoichiometric zirconium carbides, *Strength of Materials* 5 (1973) 1074.

- [68] J.A. Garber, A.V. Granato, Theory of the temperature dependence of second-order elastic constants in cubic materials, *Physical Review B* 11 (1975) 3990.
- [69] Y.P. Varshni, Temperature dependence of the elastic constants, *Physical Review B* 2 (1970) 3952.
- [70] J.L. Tallon, A. Wolfenden, Temperature-dependence of the elastic-constants of aluminum, *Journal of Physics and Chemistry of Solids* 40 (1979) 831.
- [71] W.S. Williams, Transition-metal carbides, *Progress in solid state chemistry* 6 (1971) 57.
- [72] L. Huang, M. Ramzan, L. Vitos, B. Johansson, R. Ahuja, Anomalous temperature dependence of elastic constant C_{44} in V, Nb, Ta, Pd, and Pt, *Journal of Physics and Chemistry of Solids* 71 (2010) 1065.
- [73] P. Keuter, D. Music, V. Schnabel, M. Stuer, J.M. Schneider, From qualitative to quantitative description of the anomalous thermoelastic behavior of V, Nb, Ta, Pd and Pt, *Journal of Physics-Condensed Matter* 31 (2019) 22.
- [74] S. Kiani, C. Ratsch, A.M. Minor, J.M. Yang, S. Kodambaka, In situ transmission electron microscopy observations of room-temperature plasticity in sub-micron-size TaC(100) and TaC(011) single crystals, *Scripta Materialia* 100 (2015) 13.
- [75] Z.C. Wang, M. Saito, K.P. McKenna, Y. Ikuhara, Polymorphism of dislocation core structures at the atomic scale, *Nature Communications* 5 (2014) 3239.
- [76] E. Maras, M. Saito, K. Inoue, H. Jonsson, Y. Ikuhara, K.P. McKenna, Determination of the structure and properties of an edge dislocation in rutile TiO_2 , *Acta Materialia* 163 (2019) 199.
- [77] Y. Furushima, Y. Arakawa, A. Nakamura, E. Tochigi, K. Matsunaga, Nonstoichiometric 012 dislocation in strontium titanate, *Acta Materialia* 135 (2017) 103.
- [78] R. von Mises, Mechanik der plastischen Formänderung von Kristallen, *Zeitschrift für Angewandte Mathematik und Mechanik* 8 (1928) 161.
- [79] N. De Leon, X.X. Yu, H. Yu, C.R. Weinberger, G.B. Thompson, Bonding Effects on the Slip Differences in the B1 Monocarbides, *Physical Review Letters* 114 (2015) 165502.
- [80] K. Kaufmann, D. Maryanovsky, W.M. Mellor, C. Zhu, A.S. Rosengarten, T.J. Harrington, C. Oses, C. Toher, S. Curtarolo, K.S. Vecchio, Discovery of high-entropy ceramics via machine learning, *Npj Computational Materials* 6 (2020) 42.
- [81] K. Lu, J.-X. Liu, X.-F. Wei, W. Bao, Y. Wu, F. Li, F. Xu, G.-J. Zhang, Microstructures and mechanical properties of high-entropy $\text{Ti}_{0.2}\text{Zr}_{0.2}\text{Hf}_{0.2}\text{Nb}_{0.2}\text{Ta}_{0.2}\text{C}$ ceramics with the addition of SiC secondary phase, *Journal of the European Ceramic Society* 40 (2020) 1839.
- [82] C. Oses, C. Toher, S. Curtarolo, High-entropy ceramics, *Nature Reviews Materials* 5 (2020) 295.
- [83] P. Malinovskis, S. Fritze, L. Riekehr, L. von Fieandt, J. Cedervall, D. Rehnlund, L. Nyholm, E. Lewin, U. Jansson, Synthesis and characterization of multicomponent (CrNbTaTiW)C films for increased hardness and corrosion resistance, *Materials & Design* 149 (2018) 51.
- [84] H.W. Hugosson, U. Jansson, B. Johansson, O. Eriksson, Restricting dislocation movement in transition metal carbides by phase stability tuning, *Science* 293 (2001) 2434.
- [85] T. Joelsson, L. Hultman, H.W. Hugosson, J.M. Molina-Aldareguia, Phase stability tuning in the $\text{Nb}_x\text{Zr}_{1-x}\text{N}$ thin-film system for large stacking fault density and enhanced mechanical strength, *Applied Physics Letters* 86 (2005) 131922.
- [86] D.G. Sangiovanni, L. Hultman, V. Chirita, I. Petrov, J.E. Greene, Effects of phase stability, lattice ordering, and electron density on plastic deformation in cubic TiWN pseudobinary transition-metal nitride alloys, *Acta Materialia* 103 (2016) 823.
- [87] H.W. Hugosson, O. Eriksson, L. Nordstrom, U. Jansson, L. Fast, A. Delin, J.M. Wills, B. Johansson, Theory of phase stabilities and bonding mechanisms in stoichiometric and substoichiometric molybdenum carbide, *Journal of Applied Physics* 86 (1999) 3758.
- [88] A.S. Kurlov, A.I. Gusev, Tungsten carbides and W-C phase diagram, *Inorganic Materials* 42 (2006) 121.
- [89] W. Humphrey, A. Dalke, K. Schulten, VMD: Visual molecular dynamics, *Journal of Molecular Graphics & Modelling* 14 (1996) 33.

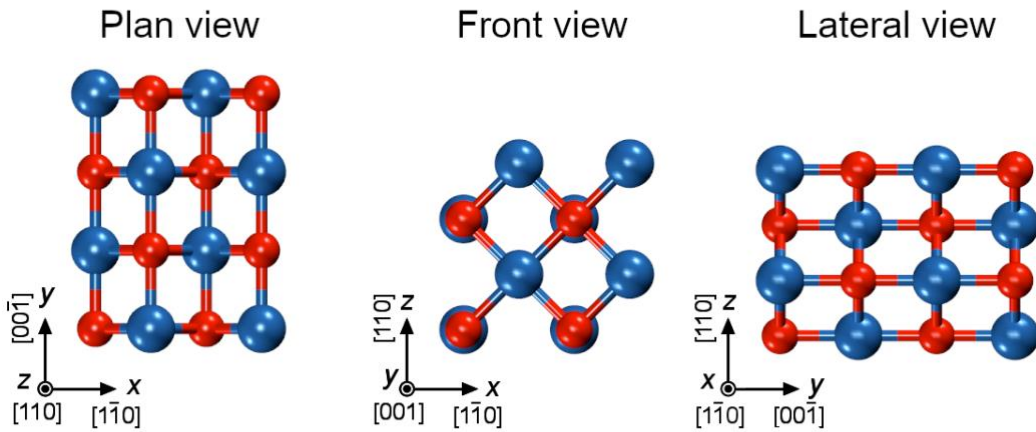
- [90] B.A. Mathe, Surface Brillouin scattering studies of elastic properties of materials at high temperature, Doctoral Thesis, University of the Witwatersrand, Johannesburg, South Africa. (2008).
- [91] B.A. Mathe, J.D. Comins, A.G. Every, W. Lengauer, Thermal dependence of elastic properties of polycrystalline $\text{TiC}_{0.97}$ and $\text{TiC}_{0.40}\text{N}_{0.60}$ alloys studied by surface Brillouin scattering, *International Journal of Refractory Metals & Hard Materials* 45 (2014) 212.
- [92] R. Chang, L.J. Graham, Low-temperature elastic properties of ZrC and TiC, *Journal of Applied Physics* 37 (1966) 3778.
- [93] L. Pintschovius, W. Reichardt, B. Scheerer, Lattice-dynamics of TiC, *Journal of Physics C-Solid State Physics* 11 (1978) 1557.
- [94] J.J. Gilman, B.W. Roberts, Elastic constants of TiC and TiB_2 , *Journal of Applied Physics* 32 (1961) 1405.
- [95] W. Pang, P.R. Stoddart, J.D. Comins, A.G. Every, D. Pietersen, P.J. Marais, Elastic properties of TiN hard films at room and high temperatures using Brillouin scattering, *International Journal of Refractory Metals & Hard Materials* 15 (1997) 179.
- [96] C. Hu, J. Huang, B.G. Sumpter, E. Meletis, T. Dumitrica, Ab Initio Predictions of Strong Interfaces in Transition-Metal Carbides and Nitrides for Superhard Nanocomposite Coating Applications, *ACS Applied Nano Materials* 1 (2018) 2029.
- [97] J.H. Richardson, Thermal expansion of three group IVA carbides to 2700°C , *Journal of the American Ceramic Society* 48 (1965) 497.
- [98] Handbook of Ceramic Hard Materials, Edited by Ralf Riedel, WILEY-VCH Verlag GmbH, D-69469 Weinheim, Germany (2000).
- [99] C.K. Jun, P.T.B. Shaffer, Elastic moduli of niobium carbide and tantalum carbide at high temperature, *Journal of the Less Common Metals* 23 (1971) 367.
- [100] R.O. Elliott, C.P. Kempter, Thermal expansion of some transition metal carbides, *The Journal of Physical Chemistry* 62 (1958) 630.
- [101] H. Yu, M. Bahadori, G.B. Thompson, C.R. Weinberger, Understanding dislocation slip in stoichiometric rocksalt transition metal carbides and nitrides, *Journal of Materials Science* 52 (2017) 6235.
- [102] S.H. Jhi, S.G. Louie, M.L. Cohen, J.W. Morris, Mechanical instability and ideal shear strength of transition metal carbides and nitrides, *Physical Review Letters* 87 (2001) 075503.
- [103] S.P. Dodd, M. Cankurtaran, B. James, Ultrasonic determination of the elastic and nonlinear acoustic properties of transition-metal carbide ceramics: TiC and TaC, *Journal of Materials Science* 38 (2003) 1107.
- [104] Shaffer, P.T.B., Plenum Press Handbook of High Temperature Materials. Materials Index Plenum Press, New York (1964).
- [105] H.L. Brown, P.E. Armstrong, C.P. Kempter, Elastic properties of some polycrystalline transition-metal monocarbides, *The Journal of Chemical Physics* 45 (1966) 547.
- [106] X. Zhang, J.D. Comins, A.G. Every, P.R. Stoddart, Surface Brillouin scattering studies on vanadium carbide, *International Journal of Refractory Metals & Hard Materials* 16 (1998) 303.
- [107] V.G. Bukatov, V.I. Knyazev, O.S. Korostin, V.M. Baranov, Temperature dependence of the Young's modulus of metallic carbides, *Inorganic Materials* 11 (1975) 310.
- [108] R.A. Andrievskii, I.I. Spivak, Strength of refractory compounds and materials based on them, *Metallurgiya: Chelyabinsk* (1989).
- [109] A.J. Kadic, K. Vucic, S. Dosenovic, D. Sapunar, L. Puljak, Extracting data from figures with software was faster, with higher interrater reliability than manual extraction, *Journal of Clinical Epidemiology* 74 (2016) 119.

Figures

TMC(001)



TMC(110)



TMC(111)

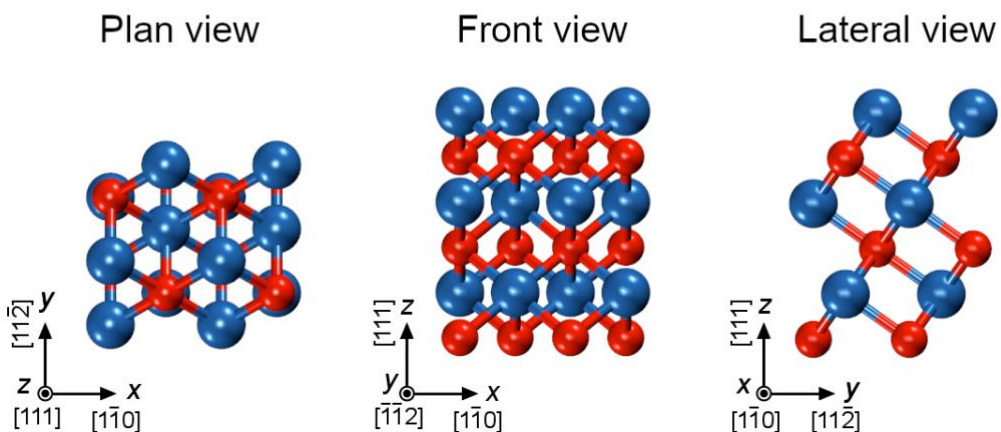


Fig. 1. Illustration of the building blocks used to generate supercell models with three different vertical (z) orientations, i.e., $[001]$, $[110]$, and $[111]$. Note that the actual supercells used in our AIMD simulations of tensile and shear deformation contain 576 atoms each (see figure 1 in [33]). Spheres of different colors indicate the metal and carbon sites of the B1 crystal structure. This figure is generated using the VMD software [89].

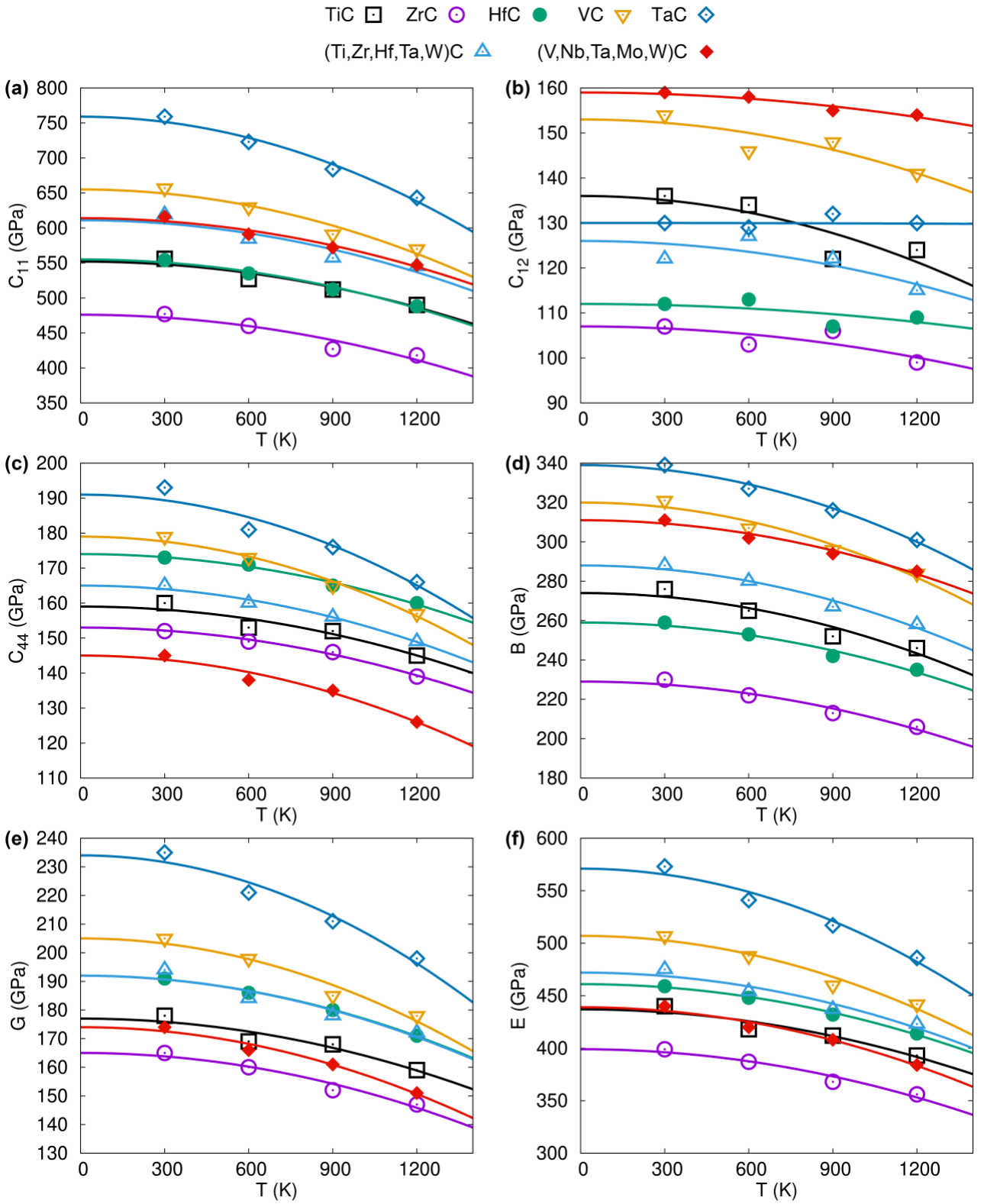


Fig. 2. (a) C_{11} , (b) C_{12} , (c) C_{44} elastic constants, bulk (d) B, shear (e) G, and (f) Young E moduli (open and filled symbols) of B1 carbides as a function of temperature calculated via AIMD. The solid lines, which serve as guide to the eye, are 2nd order polynomials obtained by imposing zero slope at 0 K and least-squares differences with the elastic properties determined by AIMD. The statistical uncertainty on the calculated elastic properties is of the order of the pressure differences between symbols and corresponding lines.

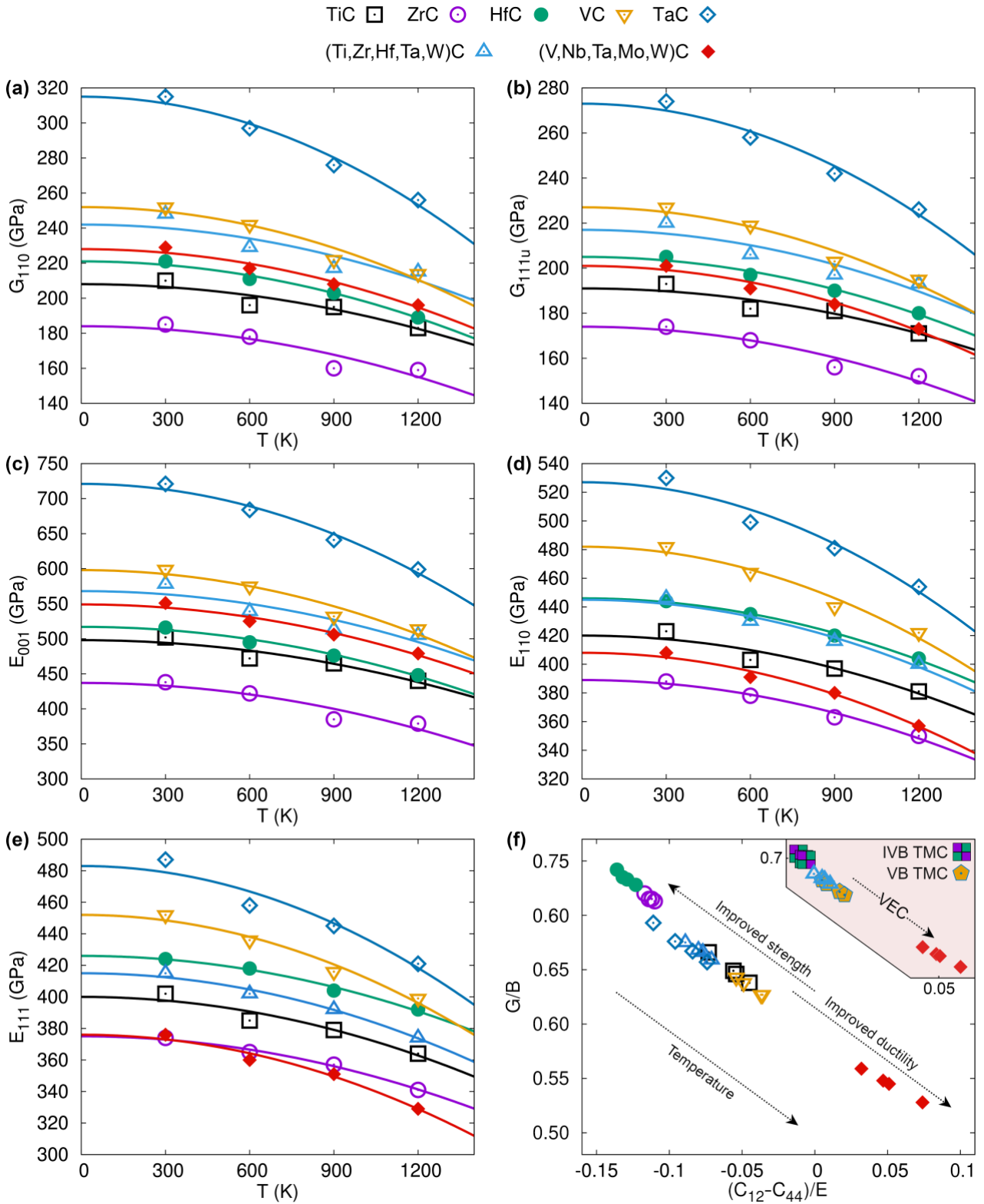


Fig. 3. Shear elastic stiffnesses (a) G_{110} and (b) G_{111u} , directional Youngs moduli (c) E_{001} , (d) E_{110} , and (e) E_{111} (open and filled symbols) and (f) ductility vs. strength maps based on phenomenological elastic-moduli-based indicators [7, 12] of B1 carbides as a function of temperature calculated via AIMD. The solid lines, which serve as guide to the eye, are 2nd order polynomials obtained by imposing zero slope at 0 K and least-squares differences with the elastic properties determined by AIMD. The statistical uncertainty on the calculated elastic properties is of the order of the difference in pressure (GPa) between a symbol and the corresponding fitted curve. In (f), the empirical criteria suggest that temperature has the general effect of improving ductility while reducing strength. However, some carbides exhibit a non-monotonic behavior in such sense (see **Tables 3–9**).

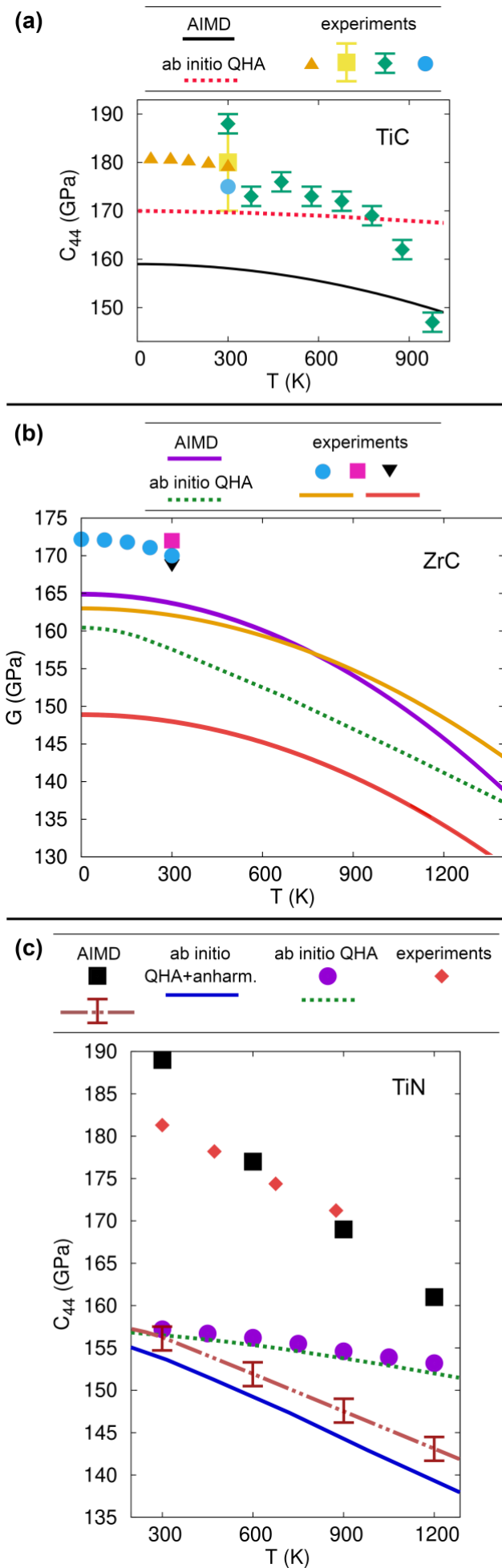


Fig. 4. Comparison between the trends in the shear elastic stiffness vs. T obtained via AIMD simulations (present work), previous *ab initio* QHA calculations [23] and experiments for different B1-structure ceramics. **(a)** C_{44} vs. T in TiC. QHA results are from Ref. [23]; experimental results for TiC_x ($x \leq 1$): green diamonds [90, 91], orange triangles [92], yellow square [93], blue circle [94]. **(b)** G vs. T in ZrC. QHA results are from Ref. [27]; experimental results for ZrC_x ($x \leq 1$): pink square [36], black triangle [36], blue circles [92], orange solid line [67] $\{B = E/[3(1-2\nu)]$ and $G = 3BE/(9B-E)\}$, red solid line [66]. **(c)** C_{44} vs. T in TiN. AIMD results of the present work are marked by black squares. Other AIMD results (red - · - line with error bars) are from Ref. [30]. *Ab initio* results that account for both thermal expansion and anharmonic effects (solid blue line) are from Ref. [28]. Results of static *ab initio* calculations: purple circles (QHA) [62] and green dotted line (volume scaling) [28]. The experimental results (red diamond) are from Ref. [95]. The figure shows that the temperature-induced decay in experimental shear elastic stiffness is better reproduced by AIMD simulations than by static *ab initio* calculations that account for thermal expansion but neglect lattice vibrations.

Tables

	$[\partial\sigma_{xx}/\partial\delta]_{\delta=0}$	$[\partial\sigma_{yy}/\partial\delta]_{\delta=0}$	$[\partial\sigma_{zz}/\partial\delta]_{\delta=0}$
Tensile deformation			
$\langle 001 \rangle$	C_{12}	C_{12}	C_{11}
$\langle 110 \rangle$	$(C_{11}+C_{12})/2-C_{44}$	C_{12}	$(C_{11}+C_{12})/2+C_{44}$
$\langle 111 \rangle$	$(C_{11}+2C_{12}-2C_{44})/3$	$(C_{11}+2C_{12}-2C_{44})/3$	$(C_{11}+2C_{12}+4C_{44})/3$
	$[\partial\sigma_{xz}/\partial\delta]_{\delta=0}$	$[\partial\sigma_{xy}/\partial\delta]_{\delta=0}$	$[\partial\sigma_{yz}/\partial\delta]_{\delta=0}$
Shear deformation			
$\{001\}\langle 1\bar{1}0 \rangle$	C_{44}	0	0
$\{110\}\langle 1\bar{1}0 \rangle$	$(C_{11}-C_{12})/2$	0	0
$\{111\}\langle 1\bar{1}0 \rangle$	$(C_{11}-C_{12}+C_{44})/3$	$(C_{11}-C_{12}-2C_{44})/(3\sqrt{2})$	0

Table 1. Correspondences between stress variations $[\partial\sigma_{ij}/\partial\delta]_{\delta=0}$ obtained during tensile or shear deformation for vanishingly small strains and second-order elastic constants of a cubic crystal. All σ_{ij} values equal 0 mean that the derivative of that σ_{ij} vs. strain component is equal zero for $\delta=0$. We note that the supercell volume and shape remain constant at each strain step of AIMD/NVT simulations. Thus, the materials' elastic resistances to $\langle 001 \rangle$, $\langle 110 \rangle$, and $\langle 111 \rangle$ elongation *do not* correspond to the directional Young's moduli E_{001} , E_{110} , E_{111} . A direct evaluation of E_{hkl} during tensile strain would require lateral supercell relaxation.

T (K)	Lattice parameter (Å)						
	TiC	ZrC	HfC	VC	TaC	(Ti,Zr,Hf,Ta,W)C	(V,Nb,Ta,Mo,W)C
0	{4.331 ^b , 4.34 ^w , 4.261–4.348 ^y , 4.297 ^f }	{4.718 ^b , 4.73 ^w , 4.685 ^f }	{4.642 ^b , 4.65 ^w , 4.608 ^f , 4.610–4.726 ^Ω }	{4.150 ^b , 4.16 ^w , 4.125 ^f }	{4.471 ^b , 4.48 ^w , 4.446 ^f , 4.435– 4.555 ^Ω }		
300	4.307 [4.318 ^q , 4.328 ^k , 4.327 ^j , 4.330 ^{tl}]	4.677 [4.683 ^q , 4.700 ^k , 4.696 ^j]	4.616 [4.637 ^k 4.641 ^j]	4.133 [4.164 ^k]	4.450 [4.454 ^q , 4.455 ^k , 4.454 ^{p*}]	4.477 [4.487 ^c]	4.370 [4.340 ^c]
600	4.317	4.687	4.625	4.143	4.460	4.487	4.379
900	4.327	4.698	4.634	4.154	4.469	4.498	4.389
1200	4.338 [4.345 ^q]	4.709 [4.715 ^q]	4.645	4.166	4.480 [4.483 ^q]	4.508	4.400
α (10 ⁻⁶ ·K ⁻¹)							
	8.0 [7.6±0.2 ^q , 8.5 ⁱ , 9.5±0.3 ^j , 8.5 ^k] {6.4 ^y }	7.6 [7.0±0.2 ^q , 7.6±0.2 ^j , 7.5 ^k , 7.5 ^e]	7.0 [7.3±0.2 ^j , 6.1 ^k]	8.9 [7.2 ^k]	7.5 [6.6±0.2 ^q , 6.3 ^k]	7.7	7.6

Table 2.* Structural parameters of TMC determined via AIMD/NPT simulations as a function of temperature. The average linear thermal expansion α is obtained for AIMD lattice parameters between 300 and 1200 K.

^Ω [96] (see supplemental material), *ab initio* calculations based on PBE and PBE with different semi-local and non-local van der Waals approximations.

^f [60], *ab initio* calculations, PBEsol functional.

^b [61], *ab initio* calculations.

^c [37], experiments for (Ti,Zr,Hf,Ta,W)C and (V,Nb,Ta,Mo,W)C.

^j [97], experiments between 300 and 3000 K for TiC_{0.73}, ZrC_{0.75}, and HfC_{0.88}.

^k [98], experiments for VC_{0.88}.

^{p*} [99], experiments for TaC_{0.99}; data refer to samples with 6% porosity.

^q [100], experiments between 300 and ≈1200 K for TiC_{0.92}, ZrC_{0.96}, and TaC_{0.98}.

^t [90], experiment: TiC_{0.97}. The average linear thermal expansion has been measured between 300 and 1600 K.

^w [101], *ab initio* calculations.

^e [65], experiments for ZrC_{0.96} and ZrC_{0.92}.

^y [23], *ab initio* calculations: the range of lattice parameters includes GGA and LDA results from Ref. [23] and *ab initio* studies referenced therein. The coefficient of thermal expansion (GGA approximation) is obtained by averaging over the values computed between 300 and 1200 K.

^{tl} [91], experiments for TiC_{0.97}. Specimen with a maximum porosity of 1.3%.

T (K)	C ₁₁ (GPa)	C ₁₂ (GPa)	C ₄₄ (GPa)	B (GPa)	G ₁₁₀ (GPa)	G _{111u} (GPa)	G _{111r} (GPa)	E ₀₀₁ (GPa)	E ₁₁₀ (GPa)	E ₁₁₁ (GPa)	G _v (GPa)	G _R (GPa)	G _H (GPa)	E _v (GPa)	E _R (GPa)	E _H (GPa)	A (%)	ν (%)	G _H /B	(C ₄₄ -C ₁₂)/E _H
0	{522 ^a , {546 ^b , 550 ^d , 509 ^e , 530 ^w , 470-606 ^y , 557 ^f }	{106 ^a , {133 ^b , 130 ^d , 146 ^e , 130 ^w , 97-130 ^y , 124 ^f }	{181 ^a , {162 ^b , 165 ^d , 168 ^e , 163 ^w , 167-230 ^y , 163 ^f }	{245 ^a , {270 ^b , 270 ^d , 267 ^e , 263 ^w , 268 ^f , 251 ^m }	{200 ^a }								{182 ^d , 183 ^f , 181 ^m }			{445 ^d , 431 ^e , 448 ^f , 438 ^m }		{23 ^d , 21 ^e , 22 ^f }	{0.71 ^e , 0.674 ^d }	
300	556 [540±30 ⁱ , 489 ^f , 477 ^h , 500 ^b , 515 ^a , {490 ^y }	136 [110±30 ⁱ , 168 ^f , 98 ^h , 113 ^b , 106 ^a , {118 ^y }	160 [180±10 ⁱ , 187 ^f , 190 ^h , 175 ^b , 179 ^a , {170 ^y }	276 [275 ^f , 224 ^h , 242 ^b , 242 ^a , 233±14 ^r , 241 ^m , 255 ^m }	210	193	190	502	423	402	180 [184±11 ^r , 186 ^m , 207 ^m , 187 ^h]	177 [184±11 ^r , 186 ^m , 207 ^m , 187 ^h]	178 [184±11 ^r , 186 ^m , 207 ^m , 187 ^h]	443 [444 ^h , 450 ^k , 436±26 ^r , 447-451 ^m , 489±13 ^m]	437 [444 ^h , 450 ^k , 436±26 ^r , 447-451 ^m , 489±13 ^m]	440 [444 ^h , 450 ^k , 436±26 ^r , 447-451 ^m , 489±13 ^m]	76	23 [19±1 ^r]	0.646	-0.054
600	527 [450 ^f , 439 ^h , {480 ^y }	134 [135 ^f , 90 ^h , {114 ^y }	153 [172 ^f , 175 ^h , {169 ^y }	265 [240 ^f , 206 ^h]	196	182	179	472	403	385	170 [173 ^h]	168 [173 ^h]	169 [173 ^h]	421 [409 ^h]	416 [409 ^h]	418 [409 ^h]	78	24	0.638	-0.045
900	512 [423 ^f , 413 ^h , {469 ^y }	122 [110 ^f , 85 ^h , {111 ^y }	152 [162 ^f , 164 ^h , {168 ^y }	252 [214 ^f , 194 ^h]	195	181	178	465	397	379	169 [163 ^h]	167 [163 ^h]	168 [163 ^h]	414 [384 ^h]	409 [384 ^h]	412 [384 ^h]	78	23	0.666	-0.073
1200	490 {457 ^y }	124 {107 ^y }	145 {166 ^y }	246	183	171	169	440	381	364	161	158	159	395 [379 ^u]	391 [379 ^u]	393 [379 ^u]	79	23	0.649	-0.056

Table 3.* Temperature-dependent elastic properties of B1 TiC.

^f [60], *ab initio* calculations (PBEsol functional).

^b [61], *ab initio* calculations.

^d [39], *ab initio* calculations. Poisson's ratio recalculated using E_H and B from ref. [39] in formula $\nu = [1 - E_H/(3B)]/2$.

^w [101], *ab initio* calculations.

^y [23], *ab initio* calculations based on quasiharmonic approximation. The range of elastic constant values includes GGA and LDA results from Ref. [23] and *ab initio* studies referenced therein.

^e [16] (see supplemental material), *ab initio* calculations.

ⁿ [102], *ab initio* calculations.

^a [92], experiments for ZrC_{0.94} and TiC_{0.91} from 8 K to room temperature.

^h [94], experiments for TiC; stoichiometry not specified.

ⁱ [93], experiments for TiC.

^j [97], experiments between 300 and 3000 K for TiC_{0.73}, ZrC_{0.75}, and HfC_{0.88}.

^q [100], experiments between 300 and ≈1200 K for TiC_{0.92}, ZrC_{0.96}, and TaC_{0.98}.

^r [103], experiments for TiC_{0.98} and TaC_{0.98} (see porosity corrected-values in table 3).

^t [90], experiments for TiC_{0.97}. Evaluation of elastic properties assumes isotropic specimen and temperature-independent Poisson's ratio.

^h [91], experiments for TiC_{0.97}. Evaluation of elastic properties assumes isotropic specimen (which has a maximum porosity of 1.3%) and temperature-independent Poisson's ratio $\nu = 0.17$.

^u [104], experiments for TiC at 1273 K.

^m [36], *ab initio* calculations and experiments + experimental references therein.

T (K)	C ₁₁ (GPa)	C ₁₂ (GPa)	C ₄₄ (GPa)	B (GPa)	G ₁₁₀ (GPa)	G _{111u} (GPa)	G _{111r} (GPa)	E ₀₀₁ (GPa)	E ₁₁₀ (GPa)	E ₁₁₁ (GPa)	G _v (GPa)	G _R (GPa)	G _H (GPa)	E _v (GPa)	E _R (GPa)	E _H (GPa)	A (%)	ν (%)	G _H /B	(C ₄₄ -C ₁₂)/E _H
0	[480] ^f , {490 ^b , 468 ^g , 474 ^w , 482 ^f , 450 ^o }	[99 ^a] {112 ^b , 123 ^g , 115 ^w , 113 ^f , 103 ^o }	[161 ^a] {147 ^b , 152 ^g , 144 ^w , 146 ^f , 153 ^o }	[226 ^a] {238 ^b , 238 ^g , 235 ^w , 236 ^f , 221 ^m }									{160 ^f , 157 ^m }			{444 ^g , 392 ^f , 381 ^m }		{19 ^g , 22 ^f }	{0.77 ^g }	
300	477 [472] ^a , {444 ^o , 435 ^o }	107 [99 ^a] {103±1 ^o }	152 [159 ^a] {153 ^o }	230 [223 ^a , 241 ^e , 220 ^m , 216 ^m]	185	174	173	438	388	374	165 [170 ^a , 148 ^s , 172 ^m , 169 ^m , 163 ^e]	164 [170 ^a , 148 ^s , 172 ^m , 169 ^m , 163 ^e]	165 [170 ^a , 148 ^s , 172 ^m , 169 ^m , 163 ^e]	400 [406 ^a , 390- 426 ^e , 346 ^s , 350 ^k , 385-406 ^m , 402±13 ^m]	397 [406 ^a , 390- 426 ^e , 346 ^s , 350 ^k , 385-406 ^m , 402±13 ^m]	399 [406 ^a , 390- 426 ^e , 346 ^s , 350 ^k , 385-406 ^m , 402±13 ^m]	82	21 [20 ^a , 23 ^e]	0.715	-0.114
600	460 {432±2 ^o , 414±2 ^o }	103 {103±7 ^o }	149 {151 ^o }	222 [239 ^e]	178	168	167	422	378	365	161 [146 ^s , 159 ^e]	159 [146 ^s , 159 ^e]	160 [146 ^s , 159 ^e]	388 [385-411 ^e , 341 ^s]	386 [385-411 ^e , 341 ^s]	387 [385-411 ^e , 341 ^s]	83	21 [23 ^e]	0.720	-0.117
900	427 {419±4 ^o , 391±4 ^o }	106 {101±9 ^o }	147 {150 ^o }	213 [235 ^e]	161	156	156	385	364	357	152 [141 ^s , 154 ^e]	152 [141 ^s , 154 ^e]	152 [141 ^s , 154 ^e]	369 [375-394 ^e , 333 ^s]	368 [375-394 ^e , 333 ^s]	368 [375-394 ^e , 333 ^s]	91	21 [24 ^e]	0.715	-0.111
1200	418 {405±6 ^o , 367±6 ^o }	99 {102±9 ^o }	139 {149 ^o }	205 [232 ^e]	160	153	152	380	350	341	147 [134 ^s , 149 ^e]	147 [134 ^s , 149 ^e]	147 [134 ^s , 149 ^e]	357 [363-383 ^e , 321 ^s]	355 [363-383 ^e , 321 ^s]	356 [363-383 ^e , 321 ^s]	87	21 [24 ^e]	0.716	-0.113

Table 4. * Temperature-dependent elastic properties of B1 ZrC.

^f [60], *ab initio* calculations (PBEsol functional).

^b [61], *ab initio* calculations.

^w [101], *ab initio* calculations.

^g [16] (see supplemental material), *ab initio* calculations.

^s [66], experiments ZrC_{0.86}. Carbon content of 10 weight% corresponds to 86% carbon occupancy of the anion sublattice in B1 ZrC.

^e [65, 67], experiments for ZrC_{0.96} and ZrC_{0.92}. B estimated as E/[3(1-2 ν)] and G = 3BE/(9B-E)

^a [92], experiments for ZrC_{0.94} and TiC_{0.91} from 8 K to room temperature.

^j [97], experiments between 300 and 3000 K for TiC_{0.73}, ZrC_{0.75}, and HfC_{0.88}.

^q [100], experiments between 300 and \approx 1200 K for TiC_{0.92}, ZrC_{0.96}, and TaC_{0.98}.

^m [36], *ab initio* calculations and experiments + experimental references therein.

^o [27], *ab initio* calculations based on quasiharmonic and quasistatic approximations.

T (K)	C ₁₁ (GPa)	C ₁₂ (GPa)	C ₄₄ (GPa)	B (GPa)	G ₁₁₀ (GPa)	G _{111u} (GPa)	G _{111r} (GPa)	E ₀₀₁ (GPa)	E ₁₁₀ (GPa)	E ₁₁₁ (GPa)	G _V (GPa)	G _R (GPa)	G _H (GPa)	E _V (GPa)	E _R (GPa)	E _H (GPa)	A (%)	v (%)	G _H /B	(C ₄₄ -C ₁₂)/E _H
0	{520 ^g , 525 ^w , 551 ^f , 540 ^b , 501 ^o }	{133 ^g , 118 ^w , 105 ^f , 112 ^b , 102 ^o }	{172 ^g , 164 ^w , 175 ^f , 171 ^b , 177 ^o }	{262 ^g , 254 ^w , 254 ^f , 255 ^b , 239 ^m }	{236 ⁿ }								{192 ^f , 186 ^m }			{395 ^g , 461 ^f , 443 ^m }		{20 ^g , 20 ^f }	{0.74 ^g }	
300	554 {496 ^o , 489 ^o }	112 {102 ^o }	173 {176±1 ^o }	259 [243 ^z , 223 ^m , 241 ^m]	221	205	202	516	444	424	192 [195 ^z , 179 ⁻ , 193 ^m , 181 ^m]	189 [195 ^z , 179 ⁻ , 193 ^m , 181 ^m]	191 [195 ^z , 179 ⁻ , 193 ^m , 181 ^m]	462 [462 ^z , 420 ^k , 316-461 ^m , 428±32 ^m]	457 [462 ^z , 420 ^k , 316-461 ^m , 428±32 ^m]	459 [462 ^z , 420 ^k , 316-461 ^m , 428±32 ^m]	78	20 [19 ^z]	0.735	-0.132
600	535 {483±3 ^o , 464±3 ^o }	113 {103±6 ^o }	171 {174±2 ^o }	253	211	197	195	495	435	418	187	185	186	450	446	448	81	20	0.733	-0.129
900	512 {467±5 ^o , 441±5 ^o }	107 {103±8 ^o }	165 {171±3 ^o }	242	203	190	189	476	420	404	180	179	180	433	430	432	82	20	0.742	-0.136
1200	488 {455±6 ^o , 416±6 ^o }	109 {103±9 ^o }	160 {170±4 ^o }	235	189	180	179	448	404	392	172	171	171	415	412	414	85	21	0.728	-0.123

Table 5.* Temperature-dependent elastic properties of B1 HfC.

^f [60], *ab initio* calculations (PBEsol functional).

^b [61], *ab initio* calculations.

^w [101], *ab initio* calculations.

^g [16] (see supplemental material), *ab initio* calculations.

ⁿ [102], *ab initio* calculations, GGA functional.

^z [105], experiments for HfC_{0.97} and TaC_{0.99}.

^j [97], experiments between 300 and 3000 K for TiC_{0.73}, ZrC_{0.75}, and HfC_{0.88}.

^z [105], experiments for HfC_{0.97} and TaC_{0.99}.

^m [36], *ab initio* calculations and experiments + experimental references therein.

^o [27], *ab initio* calculations based on quasiharmonic and quasistatic approximations.

T (K)	C ₁₁ (GPa)	C ₁₂ (GPa)	C ₄₄ (GPa)	B (GPa)	Δ (GPa)	G ₁₁₀ (GPa)	G _{111u} (GPa)	G _{111r} (GPa)	E ₀₀₁ (GPa)	E ₁₁₀ (GPa)	E ₁₁₁ (GPa)	G _v (GPa)	G _R (GPa)	G _H (GPa)	E _v (GPa)	E _R (GPa)	E _H (GPa)	A (%)	ν (%)	G _H /B	(C ₄₄ - C ₁₂)/E _H
0	{669 ^b , 648 ^g , 652 ^w , 706 ^d , 705 ^f }	{152 ^b , 170 ^g , 141 ^w , 124 ^d , 141 ^f }	{186 ^b , 189 ^g , 188 ^w , 185 ^d , 190 ^f }	{332 ^b , 329 ^g , 311 ^w , 318 ^d , 329 ^f , 283 ^m }										{222 ^d , 223 ^f , 199 ^m }			{520 ^g , 523 ^d , 546 ^f , 484 ^m }		{21 ^g , 23 ^d , 22 ^f }	{0.68 ^g , 0.674 ^d }	
300	657 [366– 527 ^v]	154 [84– 292 ^v]	179 [136– 192 ^v]	321 [250 ^m , 389 ^m]	44	252	227	222	599	482	452	208 [157 ^m , 196 ^m]	202 [157 ^m , 196 ^m]	205 [157 ^m , 196 ^m]	513 [430 ^k , 268– 420 ^m , 465±13 ^m]	501 [430 ^k , 268– 420 ^m , 465±13 ^m]	507 [430 ^k , 268– 420 ^m , 465±13 ^m]	71	24	0.638	-0.049
600	630	146	173	307	55	242	219	213	575	464	436	200	195	198	494	483	488	71	23	0.643	-0.054
900	595	148	161	297	49	224	203	198	536	434	408	186	181	183	461	451	456	72	24	0.618	-0.028
1200	533	132	156	265	76	201	186	183	481	411	392	174	172	173	429	424	426	78	23	0.651	-0.058

Table 6.* Temperature-dependent elastic properties of B1 VC.

^f [60], *ab initio* calculations (PBEsol functional).

^b [61], *ab initio* calculations.

^d [39], *ab initio* calculations. Poisson's ratio recalculated using formula $\nu = [1 - E_H/(3B)]/2$.

^w [101], *ab initio* calculations.

^g [16] (see supplemental material), *ab initio* calculations.

^k [98], experiments for VC_{0.88}.

^m [36], *ab initio* calculations and experiments + experimental references therein.

^v [106], experiments VC_x (0.75 ≤ x ≤ 0.88).

T (K)	C ₁₁ (GPa)	C ₁₂ (GPa)	C ₄₄ (GPa)	B (GPa)	G ₁₁₀ (GPa)	G _{111u} (GPa)	G _{111r} (GPa)	E ₀₀₁ (GPa)	E ₁₁₀ (GPa)	E ₁₁₁ (GPa)	G _v (GPa)	G _R (GPa)	G _H (GPa)	E _v (GPa)	E _R (GPa)	E _H (GPa)	A (%)	v (%)	G _H /B	(C ₄₄ -C ₁₂)/E _H
0	{737 ^b , 722 ^g , 685 ^w , 778 ^f }	{141 ^b , 157 ^g , 163 ^w , 128 ^f }	{175 ^b , 176 ^g , 158 ^w , 181 ^f }	{340 ^b , 345 ^g , 337 ^w , 344 ^f , 326 ^m }									{229 ^f , 213 ^m }			{553 ^g , 563 ^f , 525 ^m }		{22 ^g , 23 ^f }	{0.68 ^g }	
300	759	130	193	339 [331 ^p , 287 ^{p*} , 345 ^z , 332±39 ^f , 248-343 ^m , 219 ^m]	315	274	260	721	530	487	242 [227 ^p , 202 ^{p*} , 217 ^z , 234±27 ^f , 215-227 ^m , 184 ^m]	228 [227 ^p , 202 ^{p*} , 217 ^z , 234±27 ^f , 215-227 ^m , 184 ^m]	235 [227 ^p , 202 ^{p*} , 217 ^z , 234±27 ^f , 215-227 ^m , 184 ^m]	586 [561 ^p , 490 ^{p*} , 523 ^l , 496 ^x , 290 ^k , 538 ^z , 567±68 ^r , 241-722 ^m , 431±44 ^m]	560 [561 ^p , 490 ^{p*} , 523 ^l , 496 ^x , 290 ^k , 538 ^z , 567±68 ^r , 241-722 ^m , 431±44 ^m]	573 [561 ^p , 490 ^{p*} , 523 ^l , 496 ^x , 290 ^k , 538 ^z , 567±68 ^r , 241-722 ^m , 431±44 ^m]	61	22 [21 ^p , 24 ^z , 21±2 ^f , 21 ^x]	0.693	-0.111
600	723	129	181	327 [275 ^{p*}]	297	258	245	684	499	458	227 [187 ^{p*}]	214 [187 ^{p*}]	221 [187 ^{p*}]	554 [464 ^{p*} , 504 ^l , 484 ^x]	528 [464 ^{p*} , 504 ^l , 484 ^x]	541 [464 ^{p*} , 504 ^l , 484 ^x]	61	22 [22 ^p , 22 ^x]	0.676	-0.096
900	684	132	176	316 [273 ^{p*}]	276	242	232	641	481	445	216 [182 ^{p*}]	206 [182 ^{p*}]	211 [182 ^{p*}]	527 [448 ^{p*} , 492 ^l , 473 ^x]	507 [448 ^{p*} , 492 ^l , 473 ^x]	517 [448 ^{p*} , 492 ^l , 473 ^x]	64	23 [23 ^p , 22 ^x]	0.667	-0.084
1200	643	130	166	301 [268 ^{p*}]	256	226	217	599	454	421	202 [176 ^{p*}]	193 [176 ^{p*}]	198 [176 ^{p*}]	495 [434 ^{p*} , 480 ^l , 462 ^x]	477 [434 ^{p*} , 480 ^l , 462 ^x]	486 [434 ^{p*} , 480 ^l , 462 ^x]	65	23 [23 ^p , 22 ^x]	0.657	-0.074

Table 7.* Temperature-dependent elastic properties of B1 TaC.

^f [60], *ab initio* calculations (PBEsol functional).

^b [61], *ab initio* calculations.

^w [101], *ab initio* calculations.

^g [16] (see supplemental material), *ab initio* calculations.

^l [107] experiments for TaC_{0.99}.

^x [108] experiments for TaC_{0.95} with 3% porosity.

^z [105], experiments for HfC_{0.97} and TaC_{0.99}.

^p [99], experiments for TaC_{0.99}; data extrapolated to zero porosity.

^{p*} [99], experiments for TaC_{0.99}; data refer to samples with 6% porosity.

^q [100], experiments between 300 and ≈1200 K for TiC_{0.92}, ZrC_{0.96}, and TaC_{0.98}.

^r [103], experiments for TiC_{0.98} and TaC_{0.98} (see porosity corrected-values in table 3).

^z [105], experiments for HfC_{0.97} and TaC_{0.99}.

^m [36], *ab initio* calculations and experiments + experimental references therein.

T (K)	C ₁₁ (GPa)	C ₁₂ (GPa)	C ₄₄ (GPa)	B (GPa)	G ₁₁₀ (GPa)	G _{111u} (GPa)	G _{111r} (GPa)	E ₀₀₁ (GPa)	E ₁₁₀ (GPa)	E ₁₁₁ (GPa)	G _V (GPa)	G _R (GPa)	G _H (GPa)	E _V (GPa)	E _R (GPa)	E _H (GPa)	A (%)	v (%)	G _H /B	(C ₄₄ -C ₁₂)/E _H
0				{274 ^m }									{191 ^m }			{466 ^m }		{22 ^m }		
300	619	122	165	288 (273±17) [246 ^m]	248	220	212	578	446	415	198 (193±4) [200 ^m]	190 (193±4) [200 ^m]	194 (193±4) [200 ^m]	483 (468±3) [473±26 ^m]	468 (468±3) [473±26 ^m]	475 (468±3) [473±26 ^m]	66	22 (21±2) [18±2 ^m]	0.675	-0.089
600	584	127	160	280	229	206	200	539	430	402	187	182	184	459	448	454	70	23	0.659	-0.071
900	557	122	156	267	217	197	192	513	416	392	180	176	178	442	433	437	72	23	0.666	-0.077
1200	545	115	149	258	215	193	187	505	400	374	175	170	172	429	418	423	69	23	0.668	-0.080

Table 8.* Temperature-dependent elastic properties of B1 (Ti,Zr,Hf,Ta,W)C. The results of our present acoustic wave measurements are marked in bold and enclosed in () brackets.

^m [36], *ab initio* calculations and experiments.

T (K)	C ₁₁ (GPa)	C ₁₂ (GPa)	C ₄₄ (GPa)	B (GPa)	G ₁₁₀ (GPa)	G _{111u} (GPa)	G _{111r} (GPa)	E ₀₀₁ (GPa)	E ₁₁₀ (GPa)	E ₁₁₁ (GPa)	G _V (GPa)	G _R (GPa)	G _H (GPa)	E _V (GPa)	E _R (GPa)	E _H (GPa)	A (%)	v (%)	G _H /B	(C ₄₄ -C ₁₂)/E _H
0				{312 ^m }									{183 ^m }			{460 ^m }		{25 ^m }		
300	616	159	145	311 (269±12) [278 ^m]	229	201	192	551	408	376	178 (173±4) [226 ^m]	170 (173±4) [226 ^m]	174 (173±4) [226 ^m]	449 (426±5) [533±32 ^m]	431 (426±5) [533±32 ^m]	440 (426±5) [533±32 ^m]	63	26 (24±1) [18±2 ^m]	0.559	0.032
600	591	158	138	302	217	191	182	525	391	360	170	162	166	429	412	420	64	27	0.548	0.047
900	572	155	135	294	208	184	176	506	380	351	164	157	161	415	400	408	65	27	0.545	0.051
1200	547	154	126	285	196	173	166	479	357	329	154	147	151	392	377	384	64	28	0.528	0.074

Table 9.* Temperature-dependent elastic properties of B1 (V,Nb,Ta,Mo,W)C. The results of our present acoustic wave measurements are marked in bold and enclosed in () parentheses.

^m [36], *ab initio* calculations and experiments.

*Elastic properties evaluated in the present work by AIMD simulations are in bold. Previous *ab initio* and experimental results are reported in curly { } and square [] brackets, respectively. Several elastic properties have been extracted from plots of previous works using the open software Plot Digitizer [109].